

Spatial degrees of freedom in the context of  
distributed MIMO antenna arrays for near field  
communications

Alexander Svarvare  
alex.svarvare@gmail.com

Department of Electrical and Information Technology  
Lund University

Supervisor: Prof. Mats Gustafsson

Industrial Supervisor: Prof. Zhinong Ying

Industrial Co-Supervisor: Associate Prof. Fredrik Rusek

Examiner: Prof. Daniel Sjöberg

June 25, 2024

**SONY**



**LUNDS**  
UNIVERSITET



---

# Abstract

---

The need for speed in communications systems is increasingly prevalent in modern society, which is one of the driving factors for the evolution of new technologies. At the forefront of this evolution are Multiple-input Multiple-output (MIMO) systems. Through the usage of many antennas at the base station (BS) and user equipment (UE), significantly enhances the potential maximum data transfer rates. Central to the performance of MIMO systems is the concept of Degrees of Freedom (DoF), a metric that quantifies the controllability of a system.

This thesis examines the DoF-distribution of a MIMO-system with focus on spatial multiplexing which allows for several spatially orthogonal channels to be set up and used to increase system capacity. By identifying parameters that affect the number of DoF in the spatial domain, gives design rules and insight into simplifying the design process for future communication systems, meeting the growing demand for higher data rates.

By usage of computer simulations and the current theory of MIMO-system, this study links the effects of apparent area in the context of solid angles on the number of spatial DoF for Single-User MIMO as well as for Multiple-User MIMO. An overview of DoF-metrics is given together with novel description of a volumetric UE which extends previous low-dimensional formulations of the user together with the implementation of a real antenna model and its impact.



---

## Acknowledgements

---

I wish to show my gratitude to my academic supervisor, Mats Gustafsson, for his invaluable support in securing this thesis project at Sony and for the guidance he provided throughout its duration. Thank you Gustafsson for always leaving the door to your office slightly open and always gracefully answering my sometimes too basic questions.

I am grateful to my industrial supervisors, starting with Zhinong Ying, for his warm welcome on my first day. Additionally, I would like to express my appreciation to Fredrik Rusek for his crystal-clear explanations and effective communication. Their collective support has played a crucial role in the successful completion of this thesis.

I also wish to give a special thanks to Fellow Prof Dr Eng B.K. Lau who did not contribute to this thesis at all. He instead played a major role in shaping my academic journey by teaching the course EITF80 Electromagnetic Fields and for the internship I had with him. His impact has been lasting and significant.

I would also like to give a special thanks to Oliver and Elias for being contributors to the correctness, structure and grammar of this report.

Lastly I wish to thank the ones around me. My mother Olga, Father Janne, sister Nina, Hanna, Elias, and Jonathan who are my loved and dear.



---

# Populärvetenskaplig Sammanfattning

---

Elektromagnetiska vågor är svåra att förklara men enkla att uppleva. Det är de fotoner som träffar våra näthinnor som gör att vi ser saker. Radion plockar upp dessa för att spela nyhetsmorgon, och när wifi:t är söligt, så är det avsaknaden av dessa vågor från routern som besvärar oss.

I synnerhet är det sista exemplet något som har sett stor utveckling de senaste seklen. Den första elektriska telegrafan efterföljdes av telefonen för att sedan bli trådlös för att numera användas för att surfa på internet. Elektromagnetiska vågor är informationsbäraren i alla dessa exempel och förväntas att föra över flera hundra gånger mer information än vad de gör idag. Likt routrarna som man har i hemmet så har man basstationer utomhus som bygger upp det vi kallar för mobilnät (2G, 3G, 4G, 5G och snart 6G). Idag lägger företag och forskande instanser såsom universitet oerhört stora resurser på att forska fram hur man kan göra dessa system bättre. Ordet bättre kan betyda allt ifrån högre överföringshastigheter, snabbare responstid, bättre tillförlitlighet, mindre fysisk storlek på basstationerna till lägre energiförbrukning.

I detta examensarbete fokuserar jag på hur man kan förbättra dessa basstationer, särskilt med avseende på överföringshastighet i komplexa miljöer. Begreppet "komplex" är missvisande då det hänvisar till de vanliga miljöer vi är vana vid, exempelvis en stadsmiljö. Om man modellerar denna miljö med matematik och fysik blir formlerna oftast långa och krångliga. Detta till skillnad från triviala (enkla) miljöer där formlerna oftast blir korta och enkla. Ett exempel på en trivial miljö hade varit långt uppe i luften eller rymden där inga objekt finns så att man kan fokusera på hur en isolerad basstation fungerar.

Denna förbättring av basstationerna görs genom att med teorin om hur basstationer uppför sig, simulera dagens design i komplexa miljöer för att få reda på vad man behöver lägga krut på för att förbättra. Exempelvis är det kanske bättre att placera ut två mindre basstationer istället för bara en stor. Eller så är det kanske bättre att ändra formen på den befintliga stationen istället för att lägga till ett par extra antenner. Dessa avvägningar görs för att uppnå bästa möjliga prestanda för investeringen man gör.

Måttet som används för att bestämma om en design är bättre än en annan är antalet frihetsgrader. Dessa går att liknas med en polyglot (mångspråkig person) i ett rum där han för flera diskussioner parallellt. Den som pratar finska skriker, den som pratar svenska pratar i normal volym, den som pratar danska viskar och resten kan man knappt höra vad de säger. Om målet för polyglotten är att maximera det totala informationsflödet så är det endast mödan värt att prata med finnen, svensken och dansken. Samtidigt kan polyglotten prata oerhört snabbt med finnen då det är inga problem med att höra vad denne säger, söligare med svensken och saktast med dansken. Antalet konversationer som är värda att upprätthålla, det vill säga, bidrar positivt till det totala informationsutbytet är exakt det som kallas för antalet frihetsgrader fast i kontexten för spatiell multiplexing för kommunikationssystem med flera antenner i sändare och mottagare.

Denna uppsats har presenterat ett mer relevant mått som har i åtanke hur känslig polyglottens hörsel är. Uppsatsen har även sammanfattat den spretiga röran av nuvarande forskning på ämnet till en mer introduktionsmässig nivå och presenterar de betydande förändringar man kan göra för att förbättra designen av kommunikationssystem. Till sist har ett eget bidrag gjorts med hjälp av datorsimuleringar som visar på betydelsen för hur den upptagna ytan av ens synfält har för den spatiella multiplexingen för en såsom för flera användare.



---

## Acronyms

---

#DoF	Number of (#) Degrees of Freedom. xi, xii, 2–5, 8, 13, 15, 16, 23, 24, 27–31, 33, 37, 39, 45, 46, 50
BS	Base Station. 2–4, 27, 33, 35–37, 41, 45, 46
DoF	Degrees of Freedom. 1–4, 8, 23–25, 33, 35–37, 39–41, 45, 46, 50
EDoF	Effective Degrees of Freedom. 13
EM	ElectroMagnetic. 2, 8, 17, 31, 36, 48
FEM	Finite Element Method. 8
FOV	Field Of View. xi, 17, 39
LIS	Large Intelligent Surface. 3, 46
LOS	Line Of Sight. 36
MIMO	Multiple-input Multiple-output. xiii, 1–4, 11, 13, 20, 25, 43, 45, 46
MoM	Method of Moments. xii, 31, 32
MU-MIMO	Multiple User MIMO. 27, 43, 45
RIS	Reconfigurable Intelligent Surface. 3, 46
SISO	Single-Input Single-Output. 8
SNR	Signal to Noise Ratio. xii, 13, 14, 23, 28, 29, 45
SVD	Singular Value Decomposition. 9, 10, 12
UE	User Equipment. 2, 3, 27, 45
ULA	Uniform Linear Array. xi, xii, 17, 18, 24, 25, 31, 34–43



---

# Table of Contents

---

<b>Acronyms</b>	<b>vii</b>
<b>1 Introduction</b>	<b>1</b>
1.1 Background . . . . .	2
1.2 Purpose . . . . .	3
<b>2 Theory</b>	<b>5</b>
2.1 Notation convention and Definitions . . . . .	5
2.2 Channel model based on EM-equations . . . . .	5
2.3 Waterfilling . . . . .	11
2.4 Definition of Degrees of Freedom . . . . .	12
2.5 Introductory example . . . . .	17
<b>3 Method</b>	<b>23</b>
3.1 Examination of the different metrics used for #DoF estimation . . . . .	23
3.2 Replication of Previous Findings . . . . .	24
3.3 Examination on the effect of solid angle on the DoF-distribution and regional multiplexing for volumetric user . . . . .	24
<b>4 Results &amp; Discussion</b>	<b>27</b>
4.1 Replication of Previous Findings . . . . .	32
4.2 Examination on the effect of solid angle on the DoF-distribution & regional multiplexing for volumetric user . . . . .	33
<b>5 Conclusion &amp; Future work</b>	<b>45</b>
<b>A Maxwell's equations</b>	<b>47</b>
<b>B Farfield Definition</b>	<b>51</b>
<b>C Discretization schemes: Lebedev Quadrature</b>	<b>53</b>
<b>D Pseudo Code</b>	<b>55</b>



---

## List of Figures

---

1.1	A polyglot speaking with 100 people, all speaking to the polyglot in a different language where he can only hear three persons. . . . .	3
2.1	Illustration of applied $\mathbf{J}_s(\mathbf{r}')$ and induced currents $\mathbf{J}_r(\mathbf{r})$ coupled through a matrix $\mathbf{H}$ . . . . .	6
2.2	General structure for MIMO-channel model (Benjamin Baumgärtner [34]). . . . .	7
2.3	Visual interpretation of optimal power allocation per subchannel according to waterfilling theorem. The stabilised water-level $y = \mu$ gives the solution of how large each $x_i$ should be to maximise the problem statement in (2.11). . . . .	11
2.4	Two antennas communicating with $\hat{\mathbf{x}}$ and $\hat{\mathbf{y}}$ polarisations. . . . .	13
2.5	The setup used to derive $N_H$ in [20] which is two square planes with sidelength $\mathbf{L}$ separated by a distance $\mathbf{D}$ . . . . .	16
2.6	A visualisation of how an object which gives rise to an apparent area $\mathbf{A}$ occupies a segment of an observer's Field Of View (FOV) and results in a solid angle $\Omega$ . . . . .	17
2.7	The setup to visualise spatial multiplexing between a transmit (Tx) and receive (Rx) structure where the isotropic antennas are distributed as an Uniform Linear Array (ULA). . . . .	18
2.8	Visualisation of three significant spatial modes 1,2,3 and the 9:th for the setup defined in Fig. 2.7. . . . .	19
2.9	Mode number [1,2,3,...,9] as a percentage of the sum of all singular values ( $\mathbf{S} = \ \mathbf{H}\ _F^2$ as described in Section 2.3.1) for the setup in Fig. 2.7. . . . .	20
3.1	Visualisation of a generic geometric configuration with a transmit (Tx) and receive structure (Rx) and the solid angle $\theta$ marked between the Rx and Tx. . . . .	25
4.1	Setup for comparison of Number of (#) Degrees of Freedom (#DoF) calculated with $\Psi_e$ (2.13) and $N_H$ (2.18) for two square planes with side length $\mathbf{L}$ separated by distance $\mathbf{D}$ with $\lambda/2$ uniformly distributed points. . . . .	28

4.2	Comparison between #DoF as given by $\Psi_e$ (2.13) and $N_H$ (2.18) for different side lengths of the square apertures as given in Fig. 4.1 . . .	28
4.3	Comparison between #DoF as given by $\Psi_e$ (2.13) & $K_e$ (2.17) where " $\alpha$ dB" dictates the given Signal to Noise Ratio (SNR) for the $K_e$ metric. (a, b, c) Side lengths $[1-25 \lambda]$ for $D = 20 \lambda$ . . . . .	29
4.4	Setup for comparing $N_A$ (2.20) and $\Psi_e$ (2.13) where the inner and outer sphere are discretized according to the Lebedev-quadrature (section C). The variable $a$ is the increasing radius of the inner sphere and the outer sphere is located far enough away ( $\approx inf$ ). . . . .	30
4.5	Comparison between #DoF as given by $N_A$ (2.20) and $\Psi_e$ (2.13) for different radii $a$ measured in electrical lengths of the inner sphere using different $N$ -order of Lebedev-quadrature (section C) with the setup as defined in Fig. 4.4. . . . .	30
4.6	The setup used to visualize the difference between Green's channel model and EM-simulations for $\lambda/2$ long, $\hat{z}$ -directed dipoles (upwards). The Rx-array was rotated around the Tx-array while preserving the upwards pointing direction of the ULA. . . . .	31
4.7	The different values for $\Psi_e$ (2.13) when comparing Green's channel model with the model based on the induced currents from the electric fields as calculated by Method of Moments (MoM). The receiver of $\hat{z}$ -directed $\lambda/2$ -dipoles was swept in a circle around the transmitter while preserving the upwards pointing direction of the Rx-array as visualised in Fig. 4.6. . . . .	32
4.8	Open (above) and Closed (below) uniform distribution of points along a line. . . . .	33
4.9	EDoF $\Psi_e$ (2.13) with $N$ number of receivers and sources with <b>open</b> uniform distribution in a planar area (same setup as in Fig. 4.1) with fixed side length $L = 10\lambda_0$ at a distance $D \in [1\lambda_0, 7\lambda_0, 13\lambda_0, 19\lambda_0]$ . . . . .	33
4.10	DoF with different $N$ number of receivers and sources with <b>closed</b> uniform distribution in a planar area with fixed side length $L = 10\lambda_0$ at a distance $D \in [1\lambda_0, 7\lambda_0, 13\lambda_0, 19\lambda_0]$ . . . . .	34
4.11	Optimal number of sources/receivers calculated with the EM channel model and the intuitive method, with the side length $L = 10\lambda$ and distance $D = 1 - 13\lambda$ . . . . .	34
4.12	Square layout of a user as 4 isotropic antennas on the vertices of a two dimensional square with side length $\lambda/2$ . . . . .	35
4.13	Performance metrics for a room with rectangular geometry. . . . .	37
4.14	Performance metrics for a room with L-shaped geometry. . . . .	38
4.15	Performance metrics for a room with C-shaped geometry. . . . .	39
4.16	Total cumulative angle-iteration number calculation for boundary given in Fig. 4.15 (a) when iterating two identical ULAs. . . . .	40
4.17	Performance metrics for a room with L-shaped geometry. . . . .	40
4.18	Performance metrics for a room with rectangular geometry. . . . .	41
4.19	Performance metrics for a room with rectangular geometry. . . . .	42
4.20	Cube layout of a user as 8 isotropic antennas on the vertices of a cube with side length $\lambda/2$ . . . . .	42

4.21	Performance metrics for a room with L-shaped room for Multiple User Multiple-input Multiple-output (MIMO) case. . . . .	43
4.22	Visualisation for the three most dominant modes and least dominant mode for the square user layout. . . . .	44
B.1	Illustration of the Fraunhofer distance on how a beam has to travel longer to the edge of an aperture ( $+\Delta$ ) than to the middle of it, introducing a phase delay. . . . .	51
C.1	Theta-phi distributed points (left) and lebedev distribution (right). . . . .	54





---

## List of Tables

---

2.1	Left singular vectors for modes 1,2,3 and 9 of $\mathbf{R} = \mathbf{H}\mathbf{H}^\dagger$ for the setup in Fig. 2.7 . . . . .	19
3.1	Table of the four DoF metrics, $\Psi_e$ from (2.13), $N_H$ from (2.18), $K_e$ from (2.17) and $N_A$ from (2.20) . . . . .	23
4.1	Table with explanation for the markings in the following result-plots .	36



---

# Introduction

---

Degrees of Freedom (DoF) appears in different disciplines such as statistics, mechanics, chemistry and control theory [35]. Degrees of Freedom (DoF) refers to how many independent parameters (real-valued scalar) that describes a system.

Examples include:

1. **Statistics:** In statistics, DoF are often associated with the number of values in a calculation that are free to vary. For example, in a t-test, the DoF are related to the number of observations minus the number of constraints or conditions. In simpler terms, it represents the number of independent pieces of information available to estimate a parameter or make a comparison [6].
2. **Mechanics:** In mechanics, DoF describes the number of independent ways a rigid body can move in a given space. For example, a rigid body in three-dimensional space has six DoF: three translational DoF (movement along the  $\hat{x}$ ,  $\hat{y}$ , and  $\hat{z}$  directions) and three rotational DoF (rotation around the  $\hat{x}$ ,  $\hat{y}$ , and  $\hat{z}$  directions) [19].
3. **Chemistry:** In molecular systems, DoF represents the independent ways atoms and molecules can move or vibrate. This can include translational, rotational, and vibrational DoF [25].
4. **Control Systems:** In control theory, DoF can refer to the number of independent inputs or control parameters available to control a system [1].

Understanding DoF is crucial in various analyses and calculations, as it helps to determine the complexity of a system and the number of parameters that need to be considered for accurate modeling and analysis [1, 6, 19, 25].

In the context of MIMO-communications, using spatial multiplexing lets one utilize spatially, orthogonal communication channels to increase system capacity [7, 21, 29]. However, calculating how many useful modes exist for a certain communication setup is still an evolving area of research that warrants further investigation for comprehensive understanding [2, 38].

## 1.1 Background

DoF [21,27,31] in an ElectroMagnetic (EM) setting describes the number of useful modes that couple a source volume to a receive volume. When an applied current is put onto the source volume, an induced current on the receive volume is created that originates from the electromagnetic fields created from the currents on the source volume [20]. These coupling modes are usually referred to as EM-DoF. However, the more general acronym DoF is selected to describe useful modes within this thesis.

The term number (#) of Degrees of Freedom (#DoF) is used for describing the number of modes that positively contribute to system capacity. There exist useful modes and useless modes. For example, useful modes radiate in the correct direction and create a coupling whereas useless modes might radiate in the wrong direction. The reason we want the total number of modes to be high is because they are orthogonal, meaning that two modes with the same effectiveness (coupling strength) would increase the capacity if the transmit power was divided between those two modes [21, 27, 31]. This kind of multiplexing is more available in the nearfield (distances closer than the Fraunhofer distance, Appendix. B) which is a use case projected to be of great importance in the near future [2]. Furthermore, a capacity increase in urban environments is also possible due to the introduction of multiple path (multipath) propagation of signals which enables the Base Station (BS) to communicate with User Equipment (UE) through different spatial directions. Integration of multiple antennas into the UE, would allow it to both utilize spatial modes and to differentiate between signals coming from different spatial directions due to the reciprocity of beamforming, improving system capacity.

In the context of spatial multiplexing in MIMO-systems, the #DoF can be thought of as in the following example (Visualisation in Fig. 1.1):

A polyglot is in a room with 100 people, each speaking to the polyglot in a different language simultaneously. The first person speaking Finnish is screaming, the second speaking Swedish is talking at a normal volume, the third speaking Danish is whispering and each following person is speaking even more softly. If the objective for the polyglot is to maximize the information transferred, his energy is most well spent with the Finn, Swede and Dane. At the same time, it is beneficial to spend a little more energy speaking faster with the Finn since there is no problem hearing what the Finn is saying, spending less energy by talking at a normal pace with the Swede and even slower with the Dane. The number of conversations the polyglot upholds is the number of conversations that positively impacts the amount of information conveyed. That number is exactly the definition of #DoF in the context of spatial multiplexing for MIMO-systems. The exact formulation of this problem, on which conversations to spend energy on and how many conversations to have which maximizes the conveyed information is described by the waterfilling theorem in section 2.3.

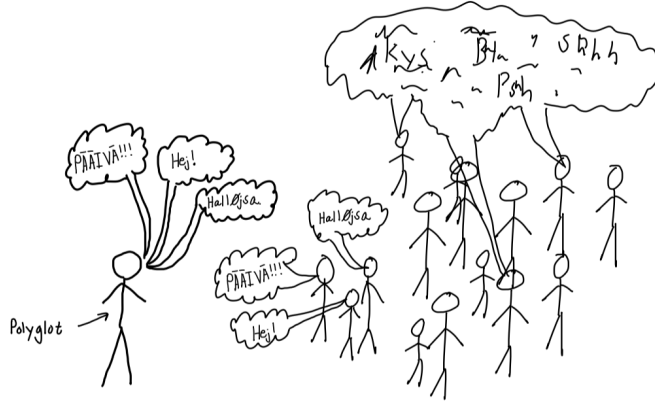


**Figure 1.1:** A polyglot speaking with 100 people, all speaking to the polyglot in a different language where he can only hear three persons.

A MIMO BS of size  $1\text{m} \times 0.5\text{m}$  and operating at 30 GHz [2], would have its Fraunhofer distance at 250 m which would indicate that the UE can no longer be considered to be in the farfield (distances greater than the Fraunhofer distance) [36] at all times. At distances greater than the Fraunhofer distance, #DoF is close to one (two if one takes into account polarisations). However, #DoF can be greater than one in the nearfield [21, 27, 31]. This speaks to the relevance of near-field communications methods.

Two emerging areas of research are the concepts of Reconfigurable Intelligent Surface (RIS) and Large Intelligent Surface (LIS), [2, 10, 11]. For example, by utilizing active and passive scattering these structures can increase capacity by extending the near-field, where multiplexing is high, to farther distances.

## 1.2 Purpose

At distances closer than the Fraunhofer distance (where phase variation over an aperture starts to become relatively large according to the derivation in Appendix. B.1), the number of useful modes (#DoF) are greater than one. Not utilizing these modes would mean missing out on channel capacity. The study of these spatial DoF, how they are distributed and the relevant parameters such as distance to UE, antenna spacing, topology and area would ensure a good level of control over the system and therefore a high-performing system [13, 21, 27, 31].

The following research questions and working objectives can be defined.

- **Objective 1:** Replication of Previous Findings

During this thesis, scientific papers were examined, their results reproduced, and conclusions drawn. The results within this thesis builds upon the same models

used in [38], and the replications of its results are provided to persuade the reader of the validity of the replicated algorithm which is available in Appendix 1.

- **Research Question 1** : Examine the different metrics used for #DoF estimation

The current literature on the study of spatial multiplexing for MIMO-systems utilizes many different formulae to calculate an approximation of the #DoF.  $\Psi_e$  is calculated from the correlation matrix  $\mathbf{R}$ .  $N_H$  approximates #DoF from the utilization of the paraxial approximation in optics ( $\sin(\theta) \approx \theta$ ) which is valid for small angles) for two square apertures pointing towards each other.  $K_e$  utilizes that the modal significance is dependent on the input power and  $N_a$  utilizes a consequence of Weyl's law [33] on the distribution of singular values for the Laplace operator [8] which relates to the average shadow area of an object (all metrics are defined in the theory section). These metrics are compared to identify impactful parameters on the DoF-distribution.

- **Research Question 2** : Examine the effect of solid angle on the DoF-distribution and regional multiplexing for volumetric users

Spatial multiplexing allows for increased capacity in MIMO-systems, and design rules to improve the availability of spatial multiplexing are sought after. With this research question, this thesis examined how the effect of solid angle between transmitter and receiver structures is significant for the utilization of spatial multiplexing.

Distributing multiple BSs gives rise to regions of high BS envelopment. This thesis examines whether this also infers regions of high spatial multiplexing. Furthermore it is examined whether the potential effect of solid angle on DoF-distribution holds for users defined as planar structures rather than volumetric users?

In this chapter, the theoretical concepts related to this thesis are presented. First, the notation conventions and definitions are presented followed by problem formulation together with the necessary theory to solve it. Afterwards, the different metrics to approximate #DoF are listed together with a new metric ( $K_e$ ) which, to the best of the author's knowledge, has not been discussed in the relevant literature. Lastly, an introductory example is presented utilizing the presented theory.

## 2.1 Notation convention and Definitions

- Vector quantities and matrices are written in boldface. For example position vector  $\mathbf{r} = x\hat{\mathbf{x}} + y\hat{\mathbf{y}} + z\hat{\mathbf{z}}$ .
- Scalar quantities are written as *italic*. For example the magnitude of the position vector  $|\mathbf{r}| = r$ .
- Position vector is, as according to convention,  $\mathbf{r}$  with source position denoted by a prime ( $'$ ). For example the distance between position vector  $\mathbf{r}$  and source position  $\mathbf{r}'$  is  $|\mathbf{r} - \mathbf{r}'|$ .
- Unit vectors are written with a hat. For example, constructing a unit vector from a vector pointing in the positive x-direction ( $x\hat{\mathbf{x}}$  with  $x > 0$ ) in  $\mathbb{R}^3$  is done as  $\frac{x\hat{\mathbf{x}}}{|x\hat{\mathbf{x}}|} = \hat{\mathbf{x}}$ .
- Solid angle [steradian] describes how much an external object occupies the field of view of an observer.
- The word "Cumulative" is an adjective that means the increase or increase in quantity, degree, or force by successive additions. An example use of the word is "cumulative angle", which refers to the summation of multiple angles.

## 2.2 Channel model based on EM-equations

The general question being asked is: given an induced current on a source volume denoted as  $\mathbf{J}_s(\mathbf{r}')$ , what is the coupling to the currents generated on the receiving

structure denoted as  $\mathbf{J}_r(\mathbf{r})$ . How this is done is through assuming that the system can be described by a coupling matrix  $\mathbf{H}$ . An illustration can be seen in Fig. 2.1. The structure of the channel matrix  $\mathbf{H}$  is decided by how one chooses to model

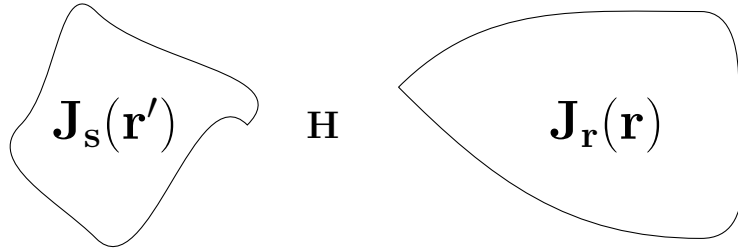


**Figure 2.1:** Illustration of applied  $\mathbf{J}_s(\mathbf{r}')$  and induced currents  $\mathbf{J}_r(\mathbf{r})$  coupled through a matrix  $\mathbf{H}$ .

the system.

### 2.2.1 Channel state information

Channel State Information (CSI) describes the properties of a communication channel. A mathematical description of a narrowband flat-fading channel model is [24]

$$\mathbf{y} = \mathbf{H}\mathbf{x} + \mathbf{n} \quad (2.1)$$

where  $\mathbf{y}$  describes the received amplitudes and phases (receive vector),  $\mathbf{x}$  describes the amplitudes and phases that we control and can put upon the transmitter (transmit vector, examples of transmit/feeding vectors are found in the columns of Table 2.1 which excite orthogonal modes),  $\mathbf{H}$  is the channel matrix which couples the transmit vector  $\mathbf{x}$  to the receive vector  $\mathbf{y}$  with the addition of some noise on the system  $\mathbf{n}$ , which is often modeled as being circular symmetric, complex, normal with  $\mathbf{n} \sim \mathcal{CN}(\mathbf{0}, \mathbf{S})$  where the mean value is zero and the noise covariance matrix  $\mathbf{S}$  is known [30].

Narrowband means that the signal occupies a narrow range of frequencies, and in this band, all frequencies experience the same fading characteristics (flat fading) [24].

The channel matrix  $\mathbf{H}$  has entries of coupling coefficients  $h_{mn}$  where there are  $N$  transmit antennas and  $M$  receive antennas as visualized in Fig. 2.2 and written in equation form without noise as



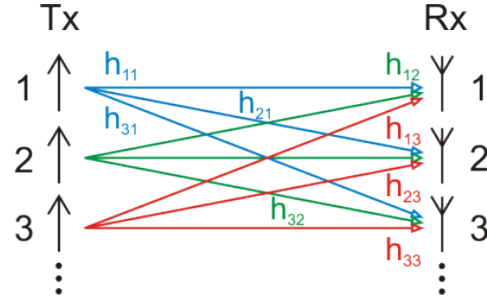


**Figure 2.2:** General structure for MIMO-channel model (Benjamin Baumgärtner [34]).

$$\begin{bmatrix} y_1 \\ y_2 \\ \vdots \\ y_M \end{bmatrix} = \begin{bmatrix} h_{11} & h_{12} & \cdots & h_{1N} \\ h_{21} & h_{22} & \cdots & h_{2N} \\ \vdots & \vdots & \ddots & \vdots \\ h_{M1} & h_{M2} & \cdots & h_{MN} \end{bmatrix} \begin{bmatrix} x_1 \\ x_2 \\ \vdots \\ x_N \end{bmatrix}.$$

## 2.2.2 Scalar Green's Function Channel Model

Utilising Green's scalar function [3], as derived in Appendix (A.29)

$$g(\mathbf{r}, \mathbf{r}') = \frac{1}{4\pi} \frac{\exp(-jk_0|\mathbf{r} - \mathbf{r}'|)}{|\mathbf{r} - \mathbf{r}'|} \quad [\text{m}^{-1}] \quad (2.2)$$

one can construct the channel matrix  $\mathbf{H}$  with  $N$  transmitters and  $M$  receivers as following

$$\mathbf{H} = \begin{bmatrix} g_{11} & g_{12} & \cdots & g_{1N} \\ g_{21} & g_{22} & \cdots & g_{2N} \\ \vdots & \vdots & \ddots & \vdots \\ g_{M1} & g_{M2} & \cdots & g_{MN} \end{bmatrix}. \quad (2.3)$$

This can be seen as distributing delta-Dirac points on the source volume, describing the amplitude of the source current at different positions (analogous to the receiving structure). In the case that the points are distributed uniformly along a line, wall or similar, the point sources are a reasonable depiction of small isotropic antennas and can give insights into the general effects and behaviours of the modes. In the case that the points are not uniformly distributed, they should be densely distributed such that each point can describe the varying amplitude of the surface current. This formulation is limited since dense sampling is not continuous, and therefore, a point described by a 3-D Dirac function with net current can be surrounded by zero current, violating Kirchhoff's current law. In that case, the formulation loses physical validity.

In normal media, the direction of the  $\mathbf{E}$  and  $\mathbf{B}$ -fields are orthogonal to the propagating direction as described by the Poynting vector [3]. Under these circumstances, for an antenna to have an isotropic radiation pattern together with a

polarisation that is not parallel to one of the radiating directions is impossible. For example, a  $\hat{\mathbf{z}}$ -directed dipole does not radiate in the  $\hat{\mathbf{z}}$ -direction. However, for acoustic signals, the propagation of the sound wave is parallel to the direction in which the increase in sound pressure travels. Due to this, the formulation of Green's channel model lacks a description of polarisation. One could utilise instances of Green's channel model to construct a formulation of co- and cross polarisation effects in a large matrix, which is the formulation of the Green Dyadic [3, 37, 38]. The instance where polarisation effects should be taken into account is when they contribute to #DoF other than when just introducing an additional dimensionality to the problem. For example when multi-path propagation can favour one polarisation over the other and enable an additional channel to the recipient.

### 2.2.3 Inclusion of basis function

Instead of describing the current on the source volume according to Green's channel model, one can instead apply basis functions which include a description of how the currents behave between the discretization points. After choosing points and basis functions, a current on the source port can be applied, E-field calculated, and coupling be computed by taking the ratio of the induced current over the applied current to achieve a coupling coefficient. This methodology is readily used when discretizing problems according to the Finite Element Method (FEM) or Method of Moments (MoM) and can also be applied to EM-problems [3, 4, 23].

### 2.2.4 Shannon Theorem

For a Single-Input Single-Output (SISO) system, the channel matrix  $\mathbf{H}$  is scalar (consists of only  $h_{11}$ ), what is the obtainable capacity? The Shannon theorem [26] describes the maximum rate information can be passed through a communication channel with a certain bandwidth in the presence of noise. It is defined as

$$C = B \log_2 \left( 1 + \frac{S}{N} \right) \quad (2.4)$$

where  $C$  is the channel capacity in  $[\frac{\text{bits}}{\text{s}}]$ ,  $B$  is the bandwidth in [Hz],  $S$  is the average received signal power over the bandwidth in [W],  $N$  is the average power of the noise and interference over the bandwidth,  $\frac{S}{N}$  is the signal-to-noise ratio (SNR) in linear-scale but usually plotted in decibel (dB).

However, this formulation does not directly give the ability to calculate what capacity is available for a communication system with multiple coupling coefficients, described by a channel matrix  $\mathbf{H}$ . The maximum attainable capacity is a property of  $\mathbf{H}$  and can be deduced by examining the #DoF that exists in the matrix, and optimally utilising them. In the case of  $\mathbf{H}$  being square, describing the matrix in terms of orthogonal DoF is precisely applying an eigenvalue-decomposition where the different eigenvectors have different eigenvalues. Generalising the eigenvalue-decomposition to non-square matrices yields the ability to calculate the capacity for non-square channel matrices. The generalisation of the eigenvalue-decomposition results in the Singular Value Decomposition (SVD).

## 2.2.5 Singular Value Decomposition (SVD)

Singular Value Decomposition (SVD) generalises the eigenvalue-decomposition to include non-square matrices [3]. It allows us to compute the capacity for a system with a coupling matrix  $\mathbf{H}$ .

Given a matrix  $\mathbf{H}$  of size  $m \times n$ , SVD decomposes it into three matrices

$$\mathbf{H} = \mathbf{U}\mathbf{\Sigma}\mathbf{V}^\dagger \quad (2.5)$$

where  $\mathbf{U}$  is an  $m \times m$  unitary matrix representing the left singular vectors,  $\mathbf{\Sigma}$  is an  $m \times n$  diagonal matrix with singular values ( $\sigma$ ) along its left diagonal,  $\mathbf{V}$  is an  $n \times n$  unitary matrix representing the right singular vectors,  $\dagger$  is the Hermitian transpose (a.k.a conjugate transpose).

There is a choice between calculating the SVD of  $\mathbf{H}$  or the correlation matrix  $\mathbf{R} = \mathbf{H}\mathbf{H}^\dagger$  and both are in common use. Calculating the singular values of  $\mathbf{H}$  refers to finding the transfer and receive vectors that couples to a certain mode. Calculating the SVD of  $\mathbf{R}$  has a more abstract meaning as the transmitted power of each respective antenna element is considered. Each row  $h_x$  corresponds to the coupling from antenna  $x$  to every antenna in the Rx. By calculating  $\mathbf{R} = \mathbf{H}\mathbf{H}^\dagger$  with respect to each row yields

$$\begin{aligned} & \begin{bmatrix} \boxed{h_1} \\ \boxed{h_2} \\ \vdots \\ \boxed{h_N} \end{bmatrix} \begin{bmatrix} \boxed{h_1^\dagger} & \boxed{h_2^\dagger} & \cdots & \boxed{h_N^\dagger} \end{bmatrix} \\ &= \begin{bmatrix} |h_1|^2 & h_1 h_2^\dagger & \cdots & h_1 h_N^\dagger \\ h_2 h_1^\dagger & |h_2|^2 & \cdots & h_2 h_N^\dagger \\ \vdots & \vdots & \ddots & \vdots \\ h_N h_1^\dagger & h_N h_2^\dagger & \cdots & |h_N|^2 \end{bmatrix} \end{aligned} \quad (2.6)$$

where the left diagonal in the resulting matrix now contains the square of the coupling of each antenna in Tx, which relates to its transmitted power.

The singular values of  $\mathbf{R}$  are related to the singular values of  $\mathbf{H}$  by the square. The derivation is done by computing the correlation matrix  $\mathbf{R}$  with the decomposition of  $\mathbf{H}$  as in (2.5) which yields

$$\mathbf{R} = \mathbf{U}\mathbf{\Sigma}\mathbf{V}^\dagger(\mathbf{U}\mathbf{\Sigma}\mathbf{V}^\dagger)^\dagger = \mathbf{U}\mathbf{\Sigma}\mathbf{V}^\dagger\mathbf{V}\mathbf{\Sigma}^\dagger\mathbf{U}^\dagger. \quad (2.7)$$

Since  $\mathbf{U}$  and  $\mathbf{V}$  are unitary matrices (Unitary:  $\mathbf{U}^\dagger = \mathbf{U}^{-1} \implies \mathbf{U}^\dagger \mathbf{U} = \mathbf{U} \mathbf{U}^\dagger = \mathbf{I}$ ), (2.7) can be further simplified as follows

$$\mathbf{R} = \mathbf{U} \boldsymbol{\Sigma} \boldsymbol{\Sigma}^\dagger \mathbf{U}^\dagger = \mathbf{U} \boldsymbol{\Sigma}^2 \mathbf{U}^\dagger = \mathbf{U} \begin{bmatrix} |\sigma_1|^2 & 0 & \cdots & 0 \\ 0 & |\sigma_2|^2 & \cdots & 0 \\ \vdots & \vdots & \ddots & \vdots \\ 0 & 0 & \cdots & |\sigma_N|^2 \end{bmatrix} \mathbf{U}^\dagger. \quad (2.8)$$

$\boldsymbol{\Sigma}$  contains the singular values of  $\mathbf{H}$  and  $\boldsymbol{\Sigma}^2$  contains the singular values of  $\mathbf{R}$ . Therefore they are related by the square.

In the context of spatial multiplexing, decomposing the correlation matrix allows us to compute the capacity since the singular values correspond to the coupling strength of different spatial modes.

### 2.2.6 SVD of Shannon Theorem (MIMO-capacity)

The Shannon capacity theorem can be expanded such that one can calculate the capacity for a channel matrix  $\mathbf{H}$  (MIMO-capacity [24, 38]), represented through the utilisation of SVD by singular values (channel gains)  $\sigma_i^2$ , SNR  $\rho$  and dividing the power between the modes with a factor of  $\frac{1}{n_i}$  as [24, 38]

$$C = B \cdot \sum_{i=1}^n \log_2 \left( 1 + \frac{\rho}{n_i} \sigma_i^2 \right) \quad (2.9)$$

where  $n$  is the number of non-zero singular values and  $n_i$  represents unequal power distribution.

$P_t$  is contained in  $\rho$  as  $P_t/P_n$ . By allowing for the power to be divided among the modes yields  $\frac{P_t/n_i}{P_n}$ . Assuming all modes experience the same noise characteristics. By dividing the power among  $n$  modes, one must ensure that the magnitude of  $\rho$  is preserved which is done by ensuring that  $n_i$  fulfils

$$\sum_{i=1}^n \frac{1}{n_i} = 1. \quad (2.10)$$

## 2.3 Waterfilling

Waterfilling is an algorithm [24] which solves the following constrained optimisation problem

$$\begin{aligned}
 & \max_{\{x_i\}} \sum_{i=1}^L \log(1 + x_i \lambda_i) \\
 & \text{s.t. } x_i = (\mu - \lambda_i^{-1})^+, \quad i \in \{1, 2, \dots, L\} \\
 & \quad \text{With constraints:} \\
 & \quad \sum_{i=1}^L x_i \leq P_t \\
 & \quad x_i \geq 0, \quad i \in \{1, 2, \dots, L\}
 \end{aligned} \tag{2.11}$$

where  $(x)^+$  denotes taking the positive part of the number, i.e.  $(x)^+ = \max(0, x)$ .

The formulation of the waterfilling algorithm is analogous to optimising for capacity of a MIMO-system where each  $\frac{\sigma_i^2}{n_i}$  can be mapped to a  $\lambda_i$ .

The reason why the algorithm is nicknamed waterfilling is because how the solution has a nice visual analogy depicted in Fig. 2.3. Instead of using numerical solvers, the same solution would be achieved if a water bucket with the amount of water  $P_t$  were poured into the graph. The stabilised water level  $\mu$  would be the same as the solution as achieved by the waterfilling algorithm, where in the case of the figure, only the first 3 subchannels should be used. Further details can be found in [24].

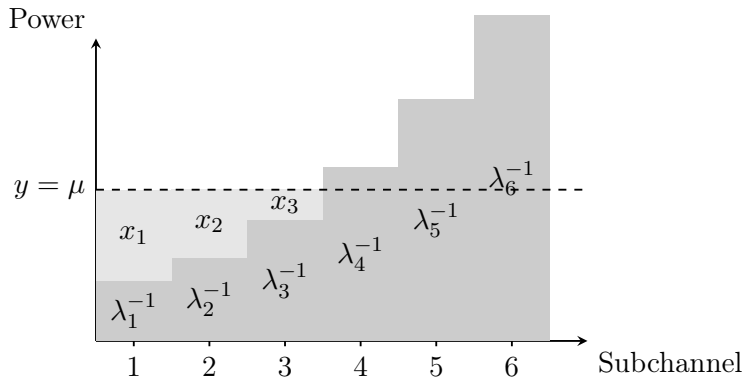


**Figure 2.3:** Visual interpretation of optimal power allocation per subchannel according to waterfilling theorem. The stabilised water-level  $y = \mu$  gives the solution of how large each  $x_i$  should be to maximise the problem statement in (2.11).

### 2.3.1 Frobenius norm and its relation to the sum of singular values of a matrix

The Frobenius norm can be used to calculate the sum of singular values  $\sigma_i$  of  $\mathbf{R} = \mathbf{H}\mathbf{H}^\dagger$  by taking the Frobenius norm of  $\mathbf{H}$  [5]

$$\|\mathbf{H}\|_F = \sqrt{\sum_i^m \sum_j^n |h_{ij}|^2} = \sqrt{\text{trace}(\mathbf{H}^\dagger \mathbf{H})} = \sqrt{\sum_{i=1}^{\min\{m,n\}} \sigma_i^2}. \quad (2.12)$$

Since the singular values for  $\mathbf{R}$  and  $\mathbf{H}$  are related by the square,  $\|\mathbf{H}\|_F$  simplifies to the square root, of the sum of the singular values of  $\mathbf{R}$ . And by taking the square of  $\|\mathbf{H}\|_F$ , gives the sum of singular values of  $\mathbf{R}$ .

By first computing the square of  $\|\mathbf{H}\|_F$ , can alleviate the calculation complexity of the SVD of  $\mathbf{R}$  such that when the current sum of already found singular values starts to approach the total sum of all singular values, one can stop the looking for new singular values since these will at most be equal to what is left of the square of  $\|\mathbf{H}\|_F$ .

## 2.4 Definition of Degrees of Freedom

In this section, the term Degrees of Freedom (DoF) is discussed and explained in the context of MIMO-communications. The following example explains the main concepts.

Imagine two antennas directed towards each other in the  $xy$ -plane, separated by a distance in  $\hat{z}$ -direction such that they can be considered to be in the farfield (Fraunhofer distance Appendix B). If one wishes to transfer as much data as possible between these, one is looking for independent basis vectors that can be used for communication. In the example, these would be the two orthogonal polarisations of the electric-field in the  $\hat{x}$  and  $\hat{y}$  directions. Another word for these bases would be Degrees of Freedom (DoF). An illustration can be seen in Fig. 2.4

The case where this is useful for MIMO-systems is spatial multiplexing [2,7,24,33] where instead of dividing the wave into orthogonal polarisations, the wave is divided into orthogonal spatial modes. This is possible due to many antennas in the transmitting and receiving structure, being able to produce and pick up on phase variations. This would allow several communication channels to be set up, analogous to how a C-note on a piano consists of its fundamental tone and overtones. A tone from the piano can be separated by applying a Fourier transform [3], and information can be transferred by coding it onto the amplitudes of each mode/overtone, allowing for multiple streams of information through one media.

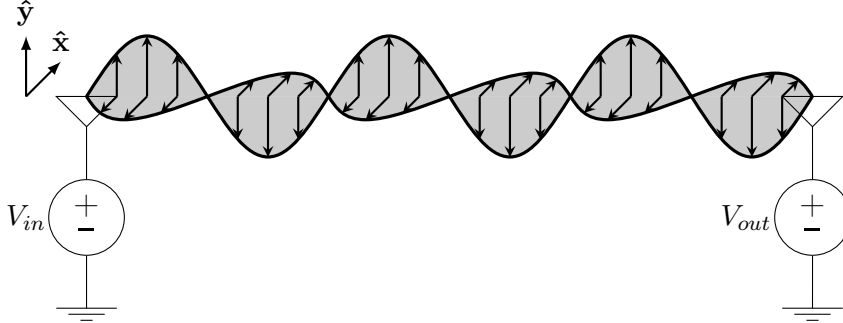


**Figure 2.4:** Two antennas communicating with  $\hat{x}$  and  $\hat{y}$  polarisations.

### 2.4.1 Metrics to estimate the number of spatial Degrees of Freedom

In a MIMO-system, spatial #DoF is defined by how many modes are used in a system after maximising capacity by applying the waterfilling algorithm. Calculating the #DoF serves as a substitute for comparing capacity since if the #DoF is greater than one, and one can facilitate the implementation, system capacity/-controllability will increase [21, 27, 31].

After computing the SVD of the correlation matrix, convention dictates that the singular values are contained in a vector where they are ordered in descending order. The nature of these modes is such that a few of the first ones are of the same magnitude and then decline sharply. The exact value for #DoF comes as a part of the solution of the accompanying waterfilling problem. If one does not wish to solve this, there are approximation methods available with varying accuracy and influential parameters. The most popular ones are listed in the following subsections where  $K_e$  presents the author's contribution on an improved metric that takes into account that the SNR should impact the #DoF.

#### Effective Degrees of Freedom (EDoF) $\Psi_e$

A common way to approximate the #DoF is [21, 27, 31]

$$\Psi_e = \left( \frac{\text{tr}(\mathbf{R})}{\|\mathbf{R}\|_F} \right)^2 = \frac{(\sum_i \sigma_i)^2}{\sum_i \sigma_i^2} \quad (2.13)$$

where  $\Psi_e$  is the EDoF and subscript e is short for effective,  $\text{tr}()$  is the matrix trace operator,  $\|\mathbf{R}\|_F$  is the Frobenius norm (2.12) and  $\sigma_i$  the singular values of  $\mathbf{R}$ .

A consequence of the introduction of EDoF  $\Psi_e$  is that the formula for the resulting capacity according to Shannon theorem (2.4) can be approximated. Assuming that all modes ( $n$ ) are orthogonal and of equal strength ( $\mathbf{R}$  is the identity matrix), Shannon theorem can be rewritten as [38]

$$C = Bn \cdot \log_2 \left( 1 + \frac{\rho}{n} \right). \quad (2.14)$$

However, this ideal case is unreachable.  $\Psi_e$  describes the number of significant modes and takes on values between  $\Psi_e \in [1, n]$ , where  $n$  is the maximum rank of  $\mathbf{R}$ . Inclusion of this instead of  $n$  yields

$$C \approx B\Psi_e \cdot \log_2 \left( 1 + \frac{\rho}{\Psi_e} \right). \quad (2.15)$$

The major drawback of (2.15) is that the SNR dictates the number of available significant modes. An explanation follows from the extension of the polyglot analogy [7, 24, 29]:

First, we need to assume that other people speaking do not contribute to how clearly the polyglot can hear the speech of another person. The polyglot, being a normal person who has normal hearing, can distinguish between the speech he is listening to from the environment as long as the person speaking does not speak too softly. If the polyglot's hearing was extremely good, he should be able to hear every person speaking in the room no matter how softly they are speaking. However, if we gave our polyglot severe tinnitus, then he might only be able to vaguely make out the Finn screaming.

With the previous extended analogy, a metric that gives the number of significant modes depending on the given SNR is described in the following section.

**DoF metric  $K_e$  by the usage of the derivative with respect to the binary logarithm**

Pouring additional water (transmitted power) into Fig. 2.3 yields a linear increase in water level up until an additional mode is included in the optimal solution for maximising capacity. After that instance, the increase in water level is slower. Since the optimal number of modes in use is reciprocal for a given optimal capacity with a set of available modes, a connection between these must exist. This is done by differentiating the capacity curve with respect to the binary log of the SNR, eliminating the binary log's influence on its appearance. What is left is how fast the water level rises with the added water, which is proportional to how many modes are in effect.

For the derivation of  $K_e$ , the derivative will be calculated as  $\frac{\partial C/B}{\partial \log_2(\rho)}$  to isolate the relation between the capacity and the sought-after number of modes being used for a given frequency. Taking the derivative is a linear operator and we focus on one term of (2.9). Therefore the derivative can be calculated using substitution as follows



$$\begin{aligned}
\frac{\partial C/B}{\partial \log_2(\rho)} &= \frac{d}{d \log_2(\rho)} \sum_{i=1}^n \log_2 \left( 1 + \frac{\rho}{n} \sigma \right) \\
&\left[ \begin{array}{l} \rho = 2^{\log_2(\rho)} \\ x = \log_2(\rho) \end{array} \right] \\
&= \frac{d}{dx} \left[ \log_2 \left( 1 + \frac{\sigma}{n} \cdot 2^x \right) \right] = \frac{d}{dx} \left[ \frac{\ln \left( \frac{\sigma \cdot 2^x}{n} + 1 \right)}{\ln(2)} \right] = \frac{1}{\ln(2)} \cdot \frac{d}{dx} \left[ \ln \left( \frac{\sigma \cdot 2^x}{n} + 1 \right) \right] \\
&= \frac{\frac{1}{\frac{\sigma \cdot 2^x}{n} + 1} \cdot \frac{d}{dx} \left[ \frac{\sigma \cdot 2^x}{n} + 1 \right]}{\ln(2)} = \frac{\frac{\sigma}{n} \cdot \frac{d}{dx} [2^x] + \frac{d}{dx} [1]}{\ln(2) \left( \frac{\sigma \cdot 2^x}{n} + 1 \right)} \\
&= \frac{\frac{\ln(2) \cdot 2^x \sigma}{n} + 0}{\ln(2) \left( \frac{\sigma \cdot 2^x}{n} + 1 \right)} = \frac{\sigma \cdot 2^x}{n \cdot \left( \frac{\sigma \cdot 2^x}{n} + 1 \right)}. \tag{2.16}
\end{aligned}$$

Simplifying, undoing the variable substitution and inclusion of all terms previously ignored, yields the final expression

$$K_e = \frac{\partial C/B}{\partial \log_2(\rho)} = \sum_{i=1}^n \frac{\sigma_i \rho}{\sigma_i \rho + n}. \tag{2.17}$$

$K_e$  can be used in place of  $\Psi_e$ , although an inspection of  $\Psi_e$  reveals that scaling of the singular values will not affect the result whereas it does for  $K_e$ . The discrepancy between the two estimates is because  $\Psi_e$  describes how many of the most well-coupled modes are on the same magnitude whereas  $K_e$  describes how many modes are significant for a specific SNR. For a very high SNR, the summation is equal to  $n$  which is the number of available modes, no matter how poorly they couple.

### #DoF $N_H$ by usage of paraxial approximation

D.A.B. Miller, through the use of the paraxial approximation in optics [20], approximates #DoF for a given setup with two planar structures separated by a distance. The approximation is provided in (2.18) and an illustration for the setup used to derive it in Fig. 2.5.

$$N_H = \frac{A_S A_R}{\lambda^2 D^2} \tag{2.18}$$

In (2.18),  $N_H$  is an approximation of #DoF,  $A$  is the area and the subindex refers to either the receive area or sender area, and  $D$  is the distance between the two planar surfaces.

Further, the formula for  $N_H$  can be rewritten by the approximation of how the surface area and solid angle relate in Fig. 2.5 as  $\Omega \approx A/D^2$ . For a general viewing angle, the area has to be reduced to apparent area. For example, a sheet of paper

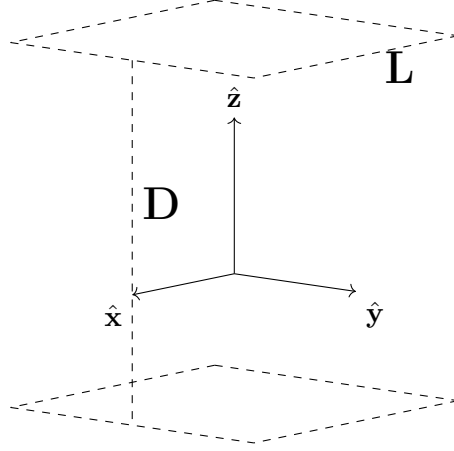


**Figure 2.5:** The setup used to derive  $N_H$  in [20] which is two square planes with sidelength  $L$  separated by a distance  $D$ .

has zero apparent area when viewed from the side and largest apparent area when viewed from the front. A visualisation is provided in Fig. 2.6.  $N_H$  can therefore be rewritten as

$$N_H \approx \Omega_S \frac{A_R}{\lambda^2} \approx \Omega_R \frac{A_S}{\lambda^2}. \quad (2.19)$$

#### #DoF $N_A$ dependent on average shadow area

In the paper [8], the authors examined the available #DoF for an arbitrary radiating structure. The differentiation between evanescent modes and radiating modes is done by punishing the amplitude of the currents on said radiating structure which physically would infer high ohmic losses, thereby suppressing those modes.

The main result is that for convex and non-convex geometries, the number of radiating modes is related by the average shadow area, which is the average shadow when illuminating an object with planar light from all directions. The average shadow area for convex objects can be simplified as  $\langle A \rangle = \frac{A}{4}$ , as originally derived by A. Cauchy [32]. Non-convex shapes have to be computed numerically.

The metric  $N_A$  can be calculated as

$$N \lesssim N_A = \frac{2k^2 \langle A_s \rangle}{\pi} \stackrel{\text{convex object}}{=} \frac{k^2 A}{2\pi} \quad (2.20)$$

where  $N$  is the total amount of modes,  $N_A$  is the #DoF,  $\langle A_s \rangle$  is the average shadow area of source object and  $A$  is the surface area of the object.

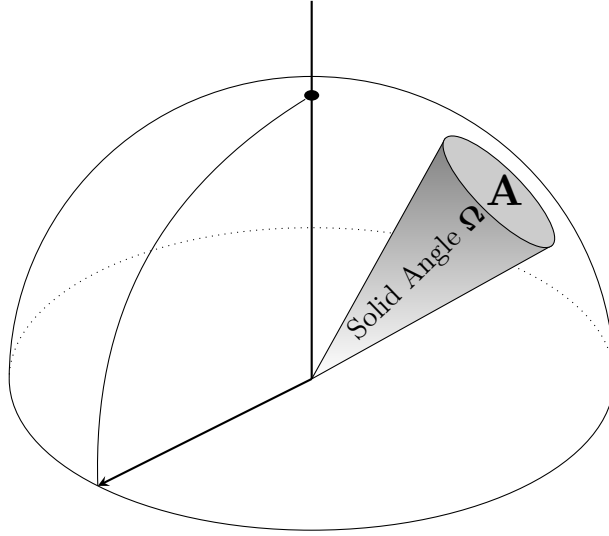


**Figure 2.6:** A visualisation of how an object which gives rise to an apparent area  $A$  occupies a segment of an observer's FOV and results in a solid angle  $\Omega$ .

## 2.5 Introductory example

A simple introductory example is constructed and presented to act as an introduction to the subject and to build up an intuition of the results presented herein.

To get an intuitive feel for spatial modes, two array structures, one for Tx and one for Rx, are constructed as 9 isotropic antennas distributed over  $4\lambda$  and separated  $4\lambda$  in distance, which means that the antennas are separated by  $\lambda/2$  as in a ULA. The setup is visualised in Fig. 2.7.

The channel matrix  $\mathbf{H}$  for the setup given in Fig. 2.7 was constructed by coupling the antennas between the transmit and receive structure by utilisation of Green's function (section 2.2.2). The singular values of the channel matrix  $\mathbf{R}$  were calculated together with the left singular vectors which excite a certain mode and the propagation of these is plotted in Fig. 2.8. For improved graphical clarity, the magnitude of the propagating EM-field were scaled with the distance the wave had travelled. Since propagating E-fields decay proportional to distance, the plotted waves do not decay. The real part of the E-field for the first three modes and the last one can be seen in Fig. 2.8 where the receive array is indicated by a gray line (to the right).

The SVD is calculated on  $\mathbf{R}$ , left singular vectors and singular values extracted. To showcase the mode significances, they are plotted in Fig. 2.9 as a percentage of the square of  $\|\mathbf{H}\|_F$ . The left singular vectors (amplitudes and phases) for modes 1,2,3 and 9 to excite orthogonal modes in the receiving structure are provided in Table 2.1. To construct the plots in Figure 2.8, each antenna in the Tx ULA

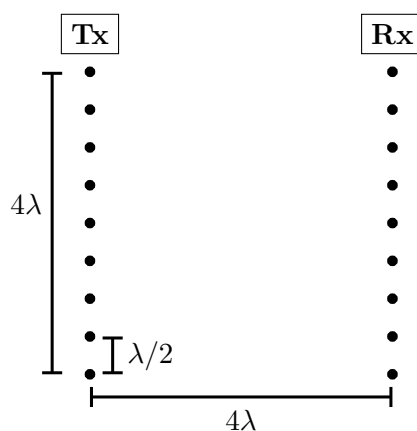


**Figure 2.7:** The setup to visualise spatial multiplexing between a transmit (Tx) and receive (Rx) structure where the isotropic antennas are distributed as an ULA.

(from top to bottom in Figure 2.7) is fed according to each row in Table 2.1 for a specific column (mode). The rows correspond to the element's position in the ULA.

The propagation, which gives rise to phase variations, is then calculated throughout the room for a given set of amplitudes and phases (mode). By superimposing the solutions for each antenna, the resulting constructive and destructive interference patterns are obtained and can be seen in Fig. 2.8.

Since pure black depicts the minimal electric field, pure white maximal electric field and grey depicts zero electric field in Fig. 2.8, the tendency for increasing modal number is a lowered amplitude of the electric-field at the receiver. Since for high modal numbers (mode 9 for instance), the electric-field tends to zero at the receiver and therefore no current is induced on the receive structure and hence, no signal. This gives an intuitive explanation for the existence of well-coupled modes and poorly coupled modes. If high order modes were to be used, the transmitted power would be directed in directions other than the receiver. Dividing the limited input energy of the transmit array among the spatial modes in an optimal way would result in an increased capacity, contrary to if only one spatial mode was used. A question posed is how many modes are available and how can they contribute to increased capacity? Also, which parameters are relevant?

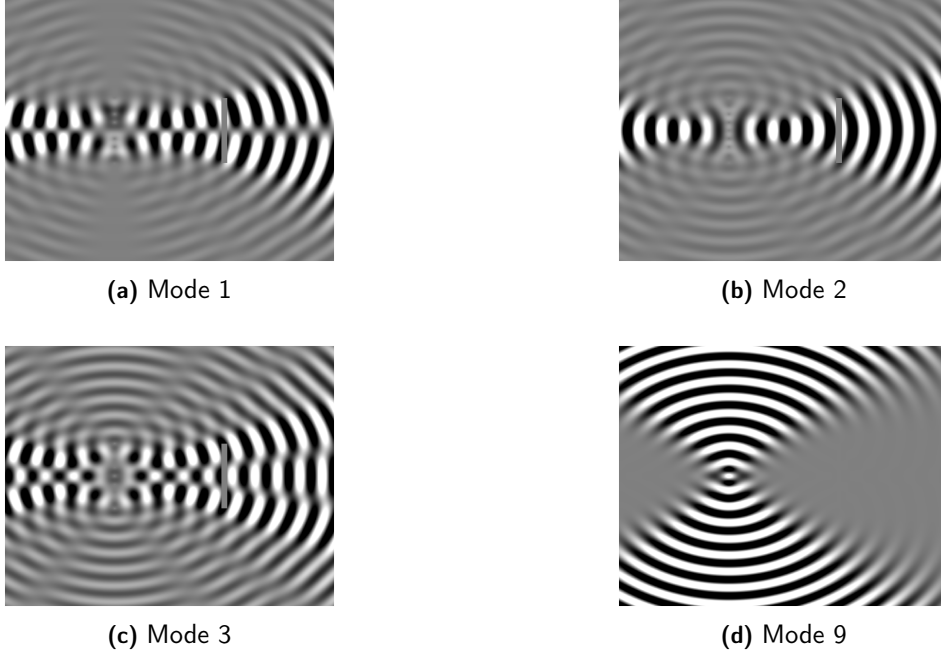


**Figure 2.8:** Visualisation of three significant spatial modes 1,2,3 and the 9:th for the setup defined in Fig. 2.7.

**Table 2.1:** Left singular vectors for modes 1,2,3 and 9 of  $\mathbf{R} = \mathbf{H}\mathbf{H}^\dagger$  for the setup in Fig. 2.7

Mode			
1	2	3	9
0.17 $\angle$ -180°	0.12 $\angle$ -180°	0.38 $\angle$ 180°	0.024 $\angle$ 0°
0.36 $\angle$ -124°	0.18 $\angle$ -101°	0.45 $\angle$ -134°	0.1206 $\angle$ -131°
0.47 $\angle$ -87°	0.30 $\angle$ -30°	0.26 $\angle$ -115°	0.30 $\angle$ 85°
0.34 $\angle$ -65°	0.46 $\angle$ 11°	0.19 $\angle$ 160°	0.49 $\angle$ -74°
0 $\angle$ -178°	0.55 $\angle$ 23°	0.34 $\angle$ 145°	0.56 $\angle$ 113°
0.34 $\angle$ 115°	0.46 $\angle$ 11°	0.19 $\angle$ 160°	0.49 $\angle$ -74°
0.47 $\angle$ 93°	0.30 $\angle$ -30°	0.26 $\angle$ -115°	0.30 $\angle$ 85°
0.36 $\angle$ 55°	0.18 $\angle$ -101°	0.45 $\angle$ -134°	0.12 $\angle$ -131°
0.17 $\angle$ 0°	0.13 $\angle$ 180°	0.40 $\angle$ -180°	0.024 $\angle$ 0°

To achieve a physical interpretation of the performance gain in capacity, we follow a structured approach by calculating the capacity with toy-example-values in two scenarios: first, using only the most strongly coupled mode, and then using waterfilling to optimize the usage of all available modes. Assuming a typical 4G frequency bandwidth of 45 MHz, 100 Watt of transmitted power and a noise floor

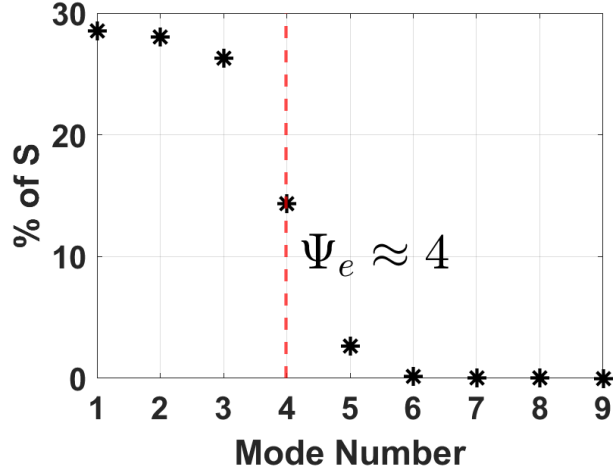


**Figure 2.9:** Mode number [1,2,3,...,9] as a percentage of the sum of all singular values ( $\mathbf{S} = \|\mathbf{H}\|_F^2$  as described in Section 2.3.1) for the setup in Fig. 2.7.

of 1 Watt. The solution can be calculated in MATLAB as following

```

1: D = [5.3e-3 5.2e-3 4.8e-3 2.6e-3 4.8e-4 2.9e-05 ...
2:       7.0e-07 6.8e-09 1.6e-11]; % Singular values of R
3: B = 45*10^6; % Bandwidth
4: Pt = 100; % Transmitted power
5: N = 1; % Noise power
6: % 20dB SNR
7: C1 = B*log2(1+D(1)/1*10^(20 / 10)) % C only 1st mode
8: waterfill(100, 1./D(1:4)); %Use first 3 modes
9: D = D(1:3);
10: P = waterfill(100, 1./D); %P-distribution over the modes
11: C2 = B*sum(log2(1+D(1:3).*(0.01*P(1:3))*10^(20 / 10)))
12: % C1 = 2.7609e+07, C2 = 3.0708e+07 -> C2/C1 = 1.1122

```

which suggests for a small scale MIMO-system as visualized in Fig. 2.7, a potential capacity increase of 11.22% is possible if spatial multiplexing is utilized. Line 10 *waterfill*( $P_t, P_n$ ) [12], applies the waterfilling algorithm for transmitted power  $P_t$  to channels with channel noises  $P_n$  and returns the optimal distribution of power  $P$  such that it optimizes the capacity  $C2$ . Assuming the same noise power (line 5) on all channels and that the efficiencies  $\lambda_i^{-1}$  handwavingly can be seen as the uneven noise power across the channels as visualized in Fig. 2.3. The vector  $D$  was sliced so that line 8 would return a readable plot. Since vector  $P$  on line 10

was set to the length of three, then it was enough to include only the first four singular values ( $D(1 : 4)$ ).





In this chapter, the method for answering the research questions and fulfilling the objectives of this thesis are presented separately (1.2).

### 3.1 Examination of the different metrics used for #DoF estimation

A comprehensive comparison of a few applicable DoF metrics is presented, enabling differentiation between their uses, validity, and influential parameters. The metrics are presented in Table. 3.1.

**Table 3.1:** Table of the four DoF metrics,  $\Psi_e$  from (2.13),  $N_H$  from (2.18),  $K_e$  from (2.17) and  $N_A$  from (2.20)

EDoF	Formula
$\Psi_e$	$\left(\frac{\text{tr}(\mathbf{R})}{\ \mathbf{R}\ _F}\right)^2 = \frac{(\sum_i \sigma_i)^2}{\sum_i \sigma_i^2}$
$N_H$	$\frac{A_S A_R}{\lambda^2 D^2}$
$K_e$	$\frac{\partial C/B}{\partial \log_2(\rho)} = \sum_{i=1}^n \frac{\sigma_i \rho}{\sigma_i \rho + n}$
$N_A$	$\frac{2k^2 \langle A_s \rangle}{\pi} \stackrel{\text{convex object}}{=} \frac{k^2 A}{2\pi}$

To enable comparisons,  $N_H$ ,  $K_e$  and  $N_A$  are paired with  $\Psi_e$  and applicable setups are created.

The  $\Psi_e$  and  $N_H$  pair was compared in a setup of two square planar transmitting and receiving arrays where different parameters from the formula for  $N_H$  are tweaked and #DoF observed.

The  $\Psi_e$  and  $K_e$  pair was measured in the same setup as the  $\Psi_e$  and  $N_H$  pair with the distance static, SNR increased and #DoF observed.

The measurement of the  $\Psi_e$  and  $N_A$  pair was conducted in a setup designed to mimic the conditions where  $N_A$  was originally introduced in [8]. This setup

involved the construction of a single sphere with an exceptionally large radius to emulate a receiver at infinity. The receiver was constructed as a small sphere, radius increased and #DoF observed.

The utilization of basis functions was studied for the  $\Psi_e$  metric in a modification of the setup in the introductory example. This was done by constructing a linear array of  $\hat{\mathbf{z}}$ -directed dipoles and computing the coupling as the induced current over the applied current. The receiving structure was swept around the transmit structure in the  $\hat{\mathbf{xz}}$ -plane to emphasize the effect of the dipole's radiation patterns effect on the  $\Psi_e$  metric while conserving the upwards direction of the ULA being swept.

### 3.2 Replication of Previous Findings

During the literature review phase of this thesis, previous results were reproduced to ensure the validity of scripts used in this report.

To validate Algorithm 1, a few of the findings in paper [38] were reproduced. Firstly two square apertures with a given sidelength separated by a distance were examined by observing the increase of the  $\Psi_e$  metric as the number of antennas on the structures increased.

Afterwards, the  $\Psi_e$  metric was measured for the same setup as in the paper [38]. The setup consisted of two sets of point sources and receivers, each consisting of 20x20 isotropic antennas, distributed uniformly on surfaces of an area of  $10 \times 10\lambda^2$ . The separating distance was then increased and its effects observed and compared with the square root of  $N_H$ .

### 3.3 Examination on the effect of solid angle on the DoF-distribution and regional multiplexing for volumetric user

In a given geometric configuration with obstructing walls, defined receive and transmit structures (visualization in Fig. 3.1), does the solid angle between those have an impact on the DoF-distribution?

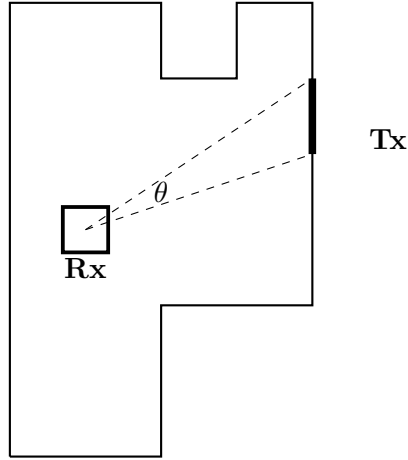


**Figure 3.1:** Visualisation of a generic geometric configuration with a transmit (Tx) and receive structure (Rx) and the solid angle  $\theta$  marked between the Rx and Tx.

Algorithm 2 was implemented as an exhaustive search of all possibilities and returned the optimal solution. The specific implementation was such that a segment of the walls of the room was allowed to be defined as two points, separated by a distance of  $100\lambda$  along the direction of **one** of the basis-vectors. Many of these wall segments were appended such that a connected structure was created. Thereafter, an ULA with the length of a half wall segment was placed along the wall at the position which maximised the solid angle (cumulative solid angle in case of multiple ULAs) to the user. Additionally, after computing the position for maximum solid angle, the user was moved around inside the room such that the resulting DoF-distribution inside of the room could be visualized.

A comprehensive series of tests were conducted, beginning with an examination of an observation point positioned in the center of a rectangular room. Subsequently, the functionality of the line-of-sight (LOS) collision code was validated using an L-shaped room. Algorithm 2 was then applied to investigate a C-shaped room for two linear arrays. The L-shaped room scenario was revisited with the observation point situated near one of the room's corners. Multiple observation points were studied within the initial rectangular room setting.

Finally, a Multiple-User MIMO (MU-MIMO) configuration was examined by choosing the ULA-placement which maximizes spatial multiplexing for a square receive topology and for a volumetric receive topology respectively.



---

## Results & Discussion

---

Firstly, pairwise comparison between the four #DoF metrics in Table 3.1 is conducted for appropriate setups and presented pairwise. The first comparison was performed between  $\Psi_e$  and  $N_H$  followed by  $\Psi_e$  and  $K_e$  in the same setup. The setup was constructed by placing two planar surfaces towards each other in  $\mathbb{R}^3$  and then computing #DoF according to the pairs. The  $\Psi_e$  and  $N_A$  pair were examined in a setup consisting of a sphere radiating out towards infinity.

Secondly, the creation of a physical antenna model (half-wavelength dipole) is included and a comparison with Green's channel model is highlighted.

Thirdly, results from [38] were reproduced and presented, intended to validate the model used within this thesis.

Fourthly, the impact of solid angle between UE and BS is examined and discussed. Lastly in the same section, a distributed Multiple User MIMO (MU-MIMO) case is examined for a planar and volumetric use case respectively.

### 4.0.1 Comparison between #DoF metrics

#### Comparison between ( $\Psi_e$ and $N_H$ ) and ( $\Psi_e$ and $K_e$ )

The setup for the comparison of  $\Psi_e$  and  $N_H$  is visualised in Fig. 4.1. It shows two square planes with side length  $L$  on which there is uniformly distributed points  $\lambda/2$  apart.

As seen from Fig. 4.2 (a),  $N_H$  and  $\Psi_e$  are similar up until the array size becomes large in comparison to the distance between the panels. For large side lengths,  $\Psi_e$  starts to stagnate whereas  $N_H$  keeps increasing. Therefore it is reasonable to suspect that  $\Psi_e$  increases with the increase of apparent area which is suggested in [8].

For small side lengths [1-5  $\lambda$ ],  $N_H$  and  $\Psi_e$  are far from similar because then  $\approx 0$ ,  $N_H \approx 0$  (since  $A_s$  and  $A_R \approx 0$ ) whereas  $\Psi_e$  is bounded by one. This is because intuitively, if the side length of the panels is zero, they can still facilitate one Delta-dirac isotropic antenna and a communication link can be created. If the

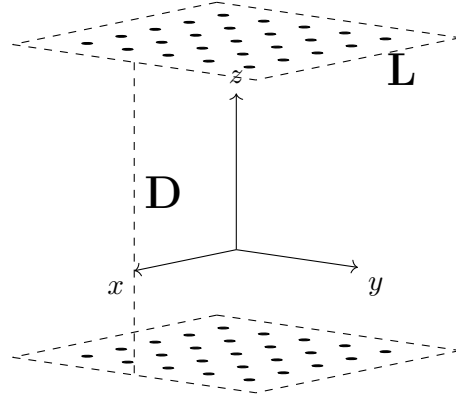


**Figure 4.1:** Setup for comparison of #DoF calculated with  $\Psi_e$  (2.13) and  $N_H$  (2.18) for two square planes with side length  $L$  separated by distance  $D$  with  $\lambda/2$  uniformly distributed points.

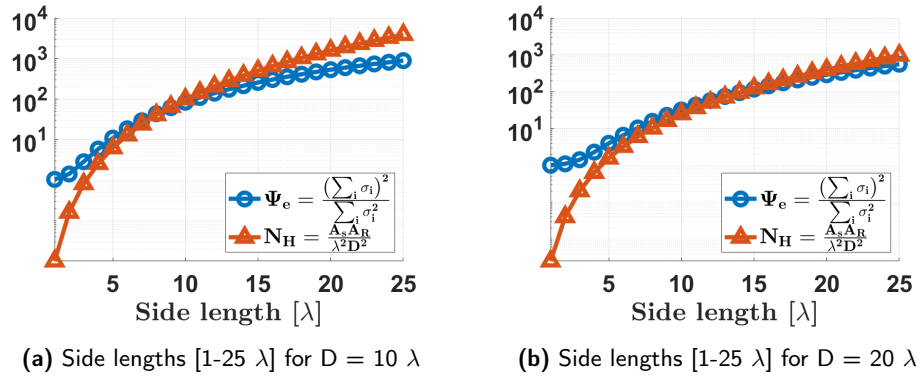


**Figure 4.2:** Comparison between #DoF as given by  $\Psi_e$  (2.13) and  $N_H$  (2.18) for different side lengths of the square apertures as given in Fig. 4.1

antenna requires an area/volume and can therefore not be placed there, then  $\Psi_e$  is undefined as  $\mathbf{H}$  will be a zero matrix.

A comparison between  $\Psi_e$  and  $K_e$  is given in Fig. 4.3 with the same setup as previously, but only for the separation of  $D = 10\lambda$ .

$\Psi_e$  normalizes away scaling of the singular values whereas  $K_e$  retains it and depending on a given SNR, computes how many of the modes are contributing. The discrepancy between  $\Psi_e$  and  $K_e$  is that the  $K_e$  curve is affected by the increase of SNR, and for very high SNR,  $\Psi_e$  and  $K_e$  starts to align. It can therefore be argued that  $\Psi_e$  assumes high SNR.

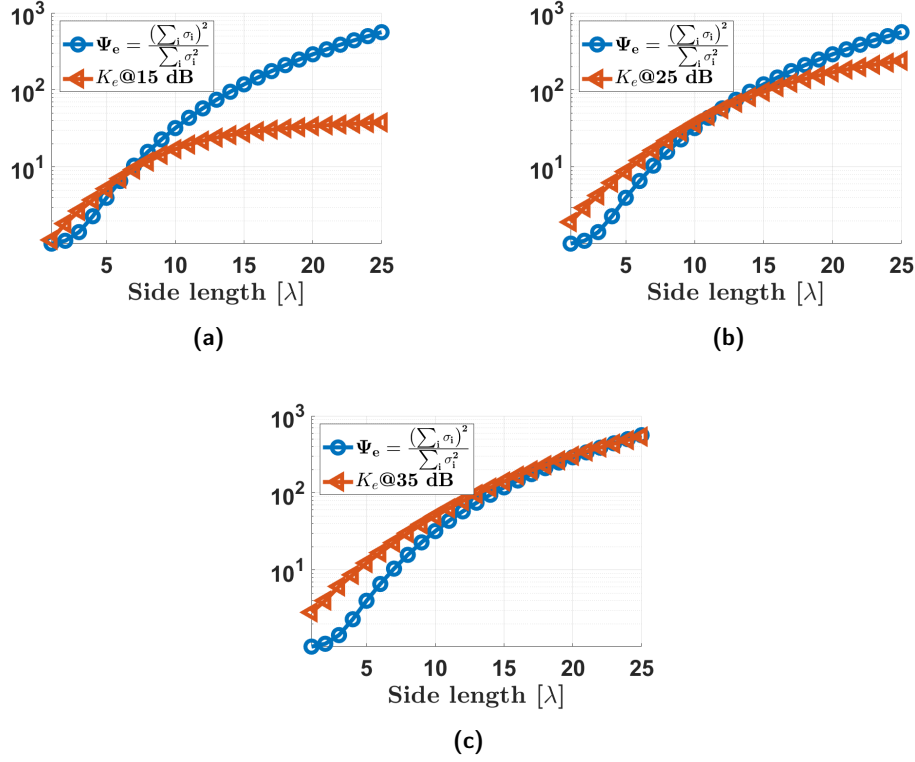


**Figure 4.3:** Comparison between #DoF as given by  $\Psi_e$  (2.13) &  $K_e$  (2.17) where " $\times$  dB" dictates the given SNR for the  $K_e$  metric. (a, b, c) Side lengths [1-25  $\lambda$ ] for  $D = 20 \lambda$ .

#### Comparison between $\Psi_e$ and $N_A$

A comparison between  $\Psi_e$  and  $N_A$  is given in Fig. 4.5. The setup consists of two spherical shells with dense sampling according to Lebedev-quadrature (Appendix. C) where the outer sphere has an extremely large radius to imitate a receiver at infinite and the inner sphere has its radius varied. Due to  $N_A$  accounting for two polarisations, the values for  $\Psi_e$  have been scaled by a factor of two. Visualisation is provided in Fig. 4.4 and results are provided in Fig. 4.5.

It was notable that  $\Psi_e$  and  $N_A$  followed the same trend but with a small difference in the gradient. This can be attributed to how the cutoff for significant modes is defined. For  $N_A$ , the authors [8] utilise a cutoff of 50 % radiation efficiency, whereas the cutoff for which modes are significant according to  $\Psi_e$  is more loose.  $\Psi_e$  returns how many of the most strongly coupled modes are on the same magnitude. Note that the increase of order in Lebedev-quadrature yields a result that corresponds more to the result of  $N_A$ . An order beyond 5294 was not pursued due to limitations of available computing power.

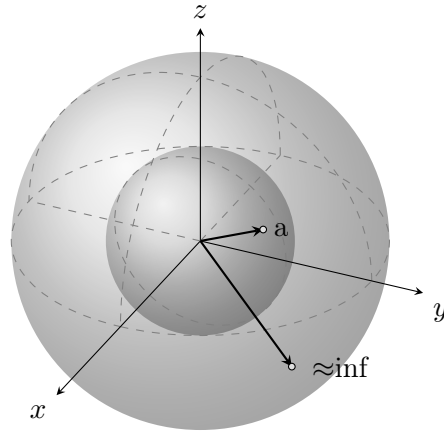


**Figure 4.4:** Setup for comparing  $N_A$  (2.20) and  $\Psi_e$  (2.13) where the inner and outer sphere are discretized according to the Lebedev-quadrature (section C). The variable  $a$  is the increasing radius of the inner sphere and the outer sphere is located far enough away ( $\approx inf$ ).

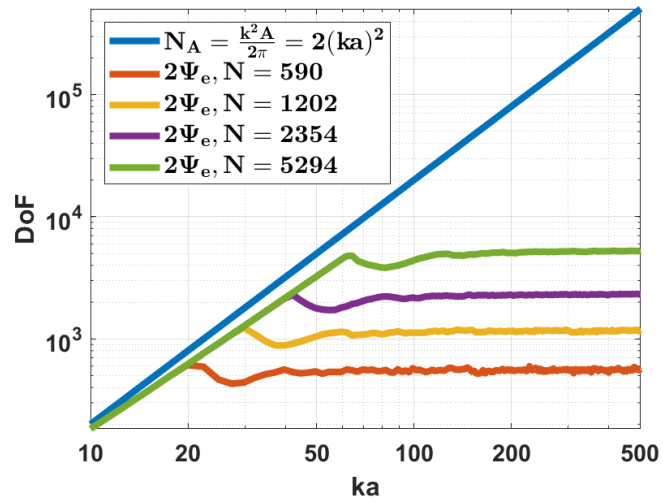


**Figure 4.5:** Comparison between #DoF as given by  $N_A$  (2.20) and  $\Psi_e$  (2.13) for different radii  $a$  measured in electrical lengths of the inner sphere using different  $N$ -order of Lebedev-quadrature (section C) with the setup as defined in Fig. 4.4.



#### 4.0.2 The effect of EM-simulations compared to Green's Function formulation

A setup as given in Fig. 4.6 was created to compare receive and transmit structures consisting of isotropic antennas (ideal, do not exist) compared to  $\hat{\mathbf{z}}$ -directed dipoles (exists in real life) respectively. For the case of isotropic antennas, the model used was Green's channel model. As for the dipoles, the coupling between the receive and transmit antennas was created by the transmitted EM-fields as computed by solving a MoM problem on the dipoles. The channel matrix's  $\mathbf{H}$  coupling coefficients were constructed as the ratio of induced currents and the applied currents in the feed of each dipole pair. The  $\Psi_e$  metric was calculating when the receiver array was swept around circularly around the transmit array while preserving the ULA's upwards pointing direction. The results can be seen in Fig. 4.7.

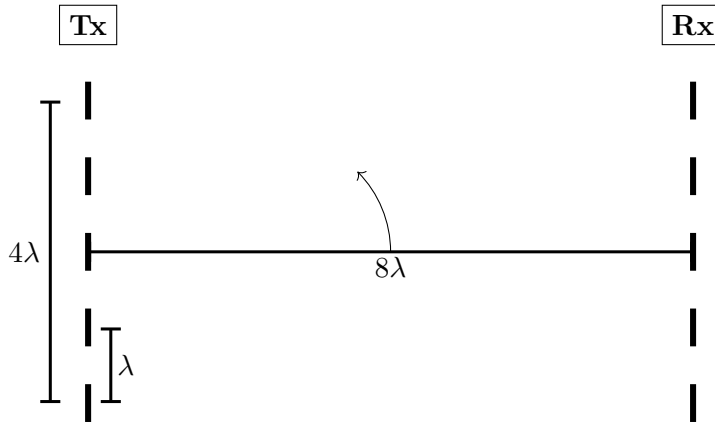


**Figure 4.6:** The setup used to visualize the difference between Green's channel model and EM-simulations for  $\lambda/2$  long,  $\hat{\mathbf{z}}$ -directed dipoles (upwards). The Rx-array was rotated around the Tx-array while preserving the upwards pointing direction of the ULA.

As shown by the different values for the  $\Psi_e$  metric in Fig. 4.6, the availability for spatial multiplexing decreases by using dipoles, compared to isotropic antennas. This reduction can be partially attributed to the introduction of the dipole's radiation pattern, which partially impairs the effectiveness of spatial multiplexing since  $\hat{\mathbf{z}}$ -directed dipoles are unable to radiate in the  $\hat{\mathbf{z}}$  direction. As per the introductory example, no electric fields implies no signal, and inhibited coupling infer reduced #DoF.

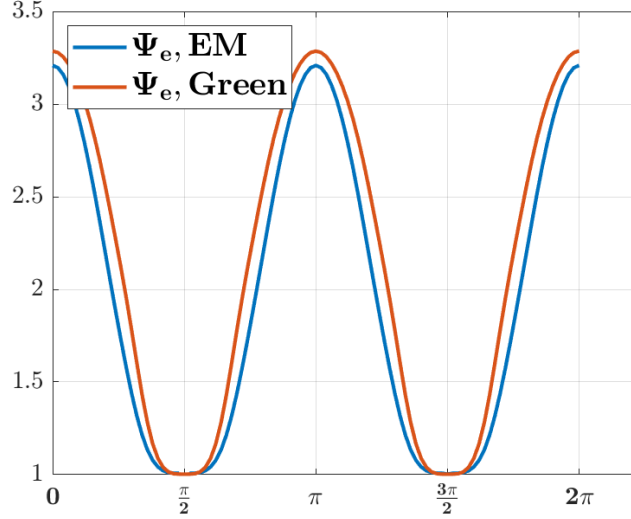


**Figure 4.7:** The different values for  $\Psi_e$  (2.13) when comparing Green's channel model with the model based on the induced currents from the electric fields as calculated by MoM. The receiver of  $\hat{z}$ -directed  $\lambda/2$ -dipoles was swept in a circle around the transmitter while preserving the upwards pointing direction of the Rx-array as visualised in Fig. 4.6.

## 4.1 Replication of Previous Findings

In this section, the interesting results from [38] will be reproduced to convince the reader of the validity of the theory and scripts used within this thesis. For the reproducibility of the results, a definition for open and closed uniform distribution needs to be made.

The phrase "Uniformly distributed" is often ill-defined for complex problems. See for example Appendix C. In antenna design, uniformly distributing  $N$  antennas over a line refers to attributing equal space to each antenna, and then placing them in the middle of their designated space. In other disciplines, the endpoints are used (this is the same as MATLAB's `linspace(start,end,#points)`) to maximise the spacing between the objects. These two definitions are henceforth referred to as open uniform distributed and closed uniform distributed respectively. Visualisations of the concepts can be found Fig. 4.8.

Firstly, Fig. 3 (a) from [38] was reproduced such that one can be sure that Algorithm 1 conforms with the algorithm used in [38]. The setup consisted of two square surfaces with a fixed side length of  $10\lambda$ , at different separating distance  $D$  (such as in Fig. 2.7). The number of antennas  $N$  according to open uniform distribution was increased and the  $\Psi_e$  metric observed. See Fig. 4.9 (a) compared

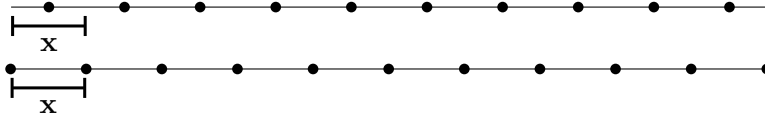


**Figure 4.8:** Open (above) and Closed (below) uniform distribution of points along a line.

to (b) for reassurance of the validity of Algorithm 1 used for the described setup.

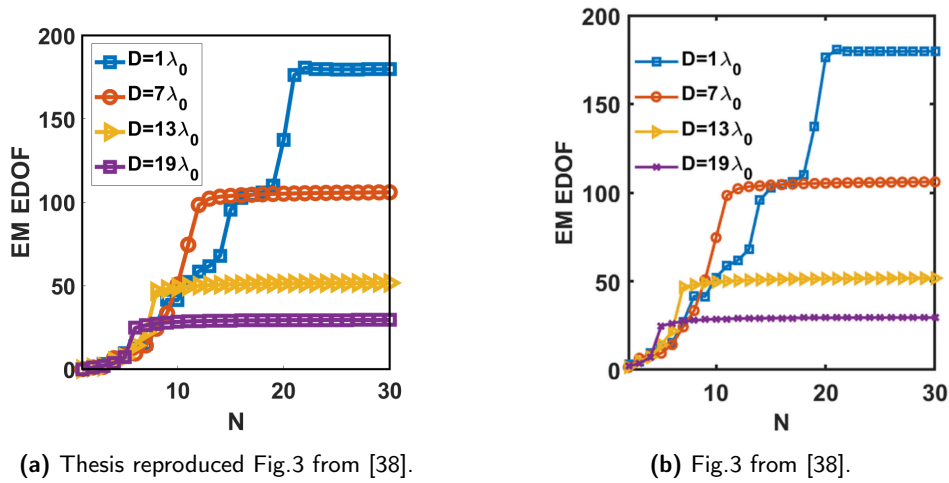


**Figure 4.9:** EDoF  $\Psi_e$  (2.13) with  $N$  number of receivers and sources with **open** uniform distribution in a planar area (same setup as in Fig. 4.1) with fixed side length  $L = 10\lambda_0$  at a distance  $D \in [1\lambda_0, 7\lambda_0, 13\lambda_0, 19\lambda_0]$ .

A design rule for the sufficient number of antenna elements needed for maximum #DoF is sought after. In Fig. 4.11, the blue line was acquired by extracting  $\text{argmax}$  (the input values that maximise a function value) from Fig. 4.10, which is similar to Fig. 4.9 in which the difference between open and closed uniform distribution is displayed. The orange line was acquired by computing the square root of  $N_H$ . The blue line can equivalently (confirmed by simulation) be obtained by utilisation of a setup with line arrays instead of surface arrays.

## 4.2 Examination on the effect of solid angle on the DoF-distribution & regional multiplexing for volumetric user

In this section, the effect of the solid angle on the DoF-distribution is examined using computer simulations. By considering different geometric setups (as visualised in Fig. 3.1) defined as rooms with different structures together with certain placements of BSs, conclusions are drawn regarding how #DoF relates to the solid

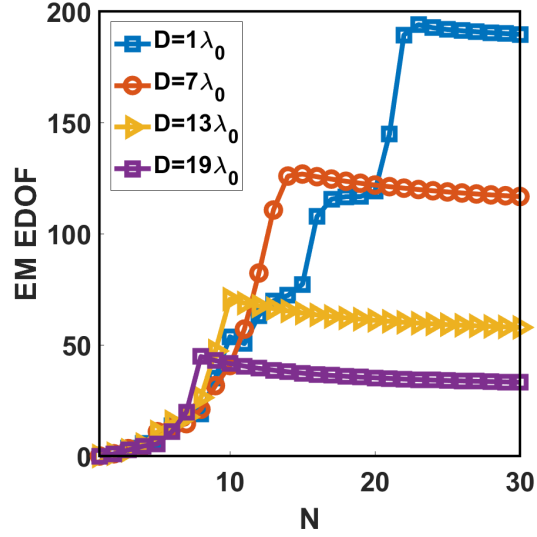
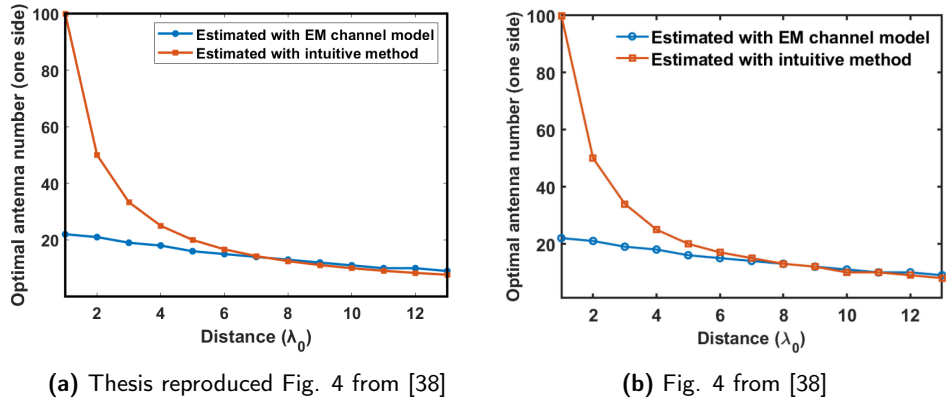


**Figure 4.10:** DoF with different  $N$  number of receivers and sources with **closed** uniform distribution in a planar area with fixed side length  $L = 10\lambda_0$  at a distance  $D \in [1\lambda_0, 7\lambda_0, 13\lambda_0, 19\lambda_0]$ .



(a) Thesis reproduced Fig. 4 from [38]

(b) Fig. 4 from [38]

**Figure 4.11:** Optimal number of sources/receivers calculated with the EM channel model and the intuitive method, with the side length  $L = 10\lambda$  and distance  $D = 1 - 13\lambda$ .

angle. By defining a Tx structure as an ULA that was put onto the walls, and sweeping said structure along the whole room for a given Rx (single/multiple user) structure inside the room, different performance metrics were computed and provided.

We started by examining two quantities. The  $\Psi_e$  metric was considered together

with the cumulative solid angle (from BS to each user). It was examined how these relate for single and multiple users in the different room structures. Lastly, different user topologies (volumetric and planar) were considered by examination of only the  $\Psi_e$  metric.

The results have the format of a (with symbol explanation in Table 4.1) room with users (red star) with angle  $\theta$  in between the markings of the angle start and end of the ULA which maximises the cumulative angle for the users. The DoF-distribution is also provided. It was calculated by sweeping one user inside the room and computing the  $\Psi_e$  metric as a measure for where multiplexing was high and low. Lastly, to verify the correctness of the solid angle calculations, a graph showing the cumulative angle calculation for each iteration of the sweeping of the BS along the walls is provided for a few cases.

For all rooms, a wall segment (orange line between two blue stars) of  $100\lambda$  was discretised with 101 points, and the length of the ULA was  $50\lambda$  with closed uniform spacing. This made the antenna spacing  $\lambda = 1$  [m] and the total amount of element per BS-ULA 51. Therefore, the iteration number symbolises a shift of  $1\lambda$  along the walls (when the graininess is 101 points), whereas for a few visualisation plots, the graininess was lowered and the meaning of the iteration number altered.

A user was represented by a small red star where Fig. 4.12 constitutes its initial layout. The DoF-distribution plots were constructed by sweeping one user across the room to visualise how available spatial multiplexing was in different parts of the room (and was therefore bounded by four as the user had four antennas). Typically the antennas are correlated in the depth dimension which results in the  $\Psi_e$  metric being at around two. This means that a wave that makes contact with two of the four vertices at the user will make the same contact with the two remaining vertices with an additional phase shift, hence no new information is available.

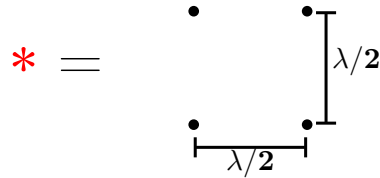






**Figure 4.12:** Square layout of a user as 4 isotropic antennas on the vertices of a two dimensional square with side length  $\lambda/2$ .

For a rectangular room according to Fig. 4.13 (a) with a user at a position at  $(100\lambda, 50\lambda)$ , the placement for an ULA with maximum angle to the user is trivial. The results can be seen in Fig. 4.13

It is observed from Fig. 4.13 (a) that for a user centred in the middle of the room, the maximum solid angle is achieved by placing the ULA in the center of the long sides of the rectangle. Fig. 4.13 (b) portrays the DoF-distribution for a user at

**Table 4.1:** Table with explanation for the markings in the following result-plots

	User
	Boundary Points
	Bounding Room
	Markings for ULA Start and End
$\theta$	Optimal Angle

different positions in the room where it is observed that multiplexing is high close to the ULA. From Fig. 4.13 (c), it is noted that there are two optimal placements.

Algorithm 2 calculates the solid angle from BS to user for each discretization point placement of the BS. Thereafter it returns the placement ( $\text{argmax}$ ) that maximises the cumulative solid-angle for all users. The optimal placement in Fig. 4.13 was for the ULA to be central to the long side of the rectangle (i.e. about  $101 \cdot 2 + 25$ ). This number is not exact since each connecting point (end of first wall, start of next wall) for two  $100\lambda$  wall segments was duplicate, and therefore two wall segments have 201 discretization points in total. The exact iteration number was  $101 \cdot 2 + 25 - 2 = 225$ .

The discrepancies for the used model compared with reality are that no multipath (created by EM-scattering on structures) effects are accounted for. It was implemented by utilising Green's channel model in free space and only interpreting the data within the boundary walls. Despite this, multipath is assumed to be an effect with lower impact than Line Of Sight (LOS) communication. This does not hold for urban environments where multipath is a dominant aspect. Even without accounting for multipath effects, conclusions can still be drawn, but it's important to recognise the limitations of the model used.

In the model used, blockages in LOS from the ULA to the user caused by obstructing walls were taken into account. If the wall obstructed a portion of the ULA, its contribution to the cumulative solid-angle was ignored. This attribute of Algorithm 2 is visualized for the room in Fig. 4.14 (a), the results of which can be seen in Fig. 4.14.

According to Fig. 4.14 (c), there exist three optimal placements where the first was utilised in the DoF-distribution calculation of the room. The effect of the user to ULA LOS obstruction caused by the wall is depicted in the same figure. Henceforth, the optimal placement is given together with its DoF-distribution without further comment.

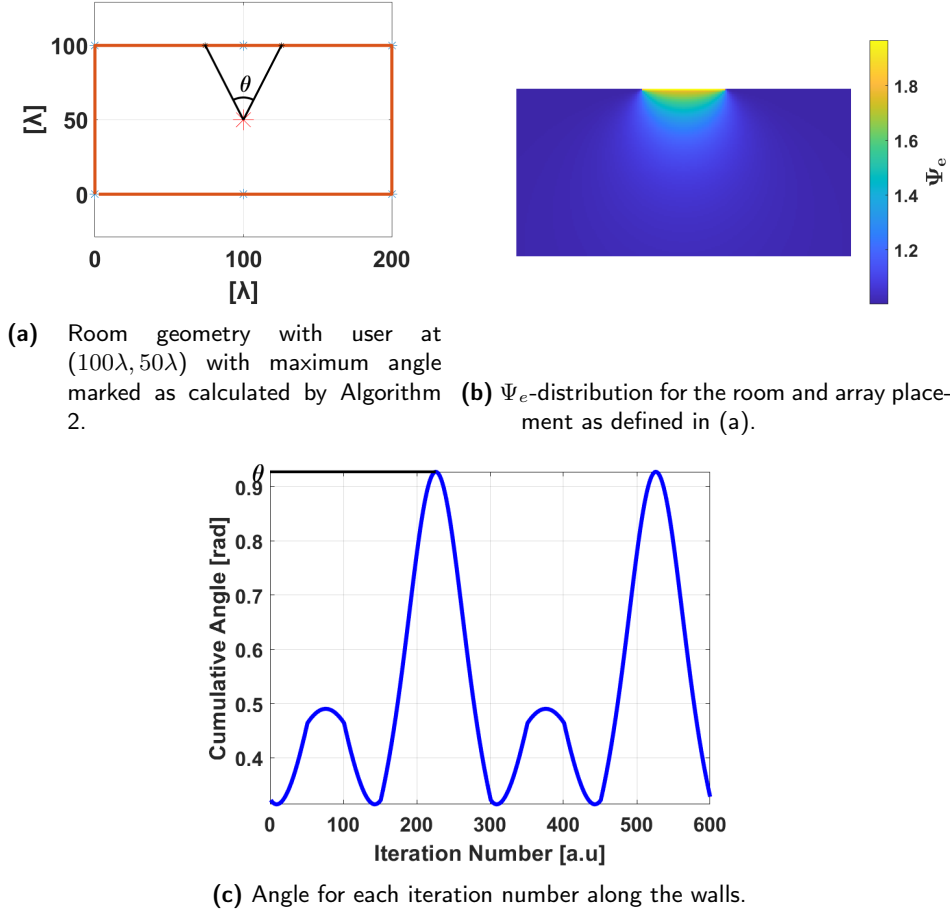


**Figure 4.13:** Performance metrics for a room with rectangular geometry.

To gain more understanding of the behaviour of the DoF-distribution, a secondary ULA was introduced. In the same manner as previously, the placement of the arrays was such that they were placed at unique locations which maximised the cumulative solid-angle to the user. This means no overlap was allowed (implemented as setting the solid-angle to zero). For the following setup, the user was placed at  $(50\lambda, 150\lambda)$ . A small segment of the active algorithm cumulative angle-iteration number is given in Fig. 4.15 (c).

As seen from the results in Fig. 4.15, the introduction of two separate BSs results in a region of high spatial multiplexing centred at the user. Therefore it can be concluded that the freedom of placing out a second BS, results in the ability to create regional areas of high #DoF.

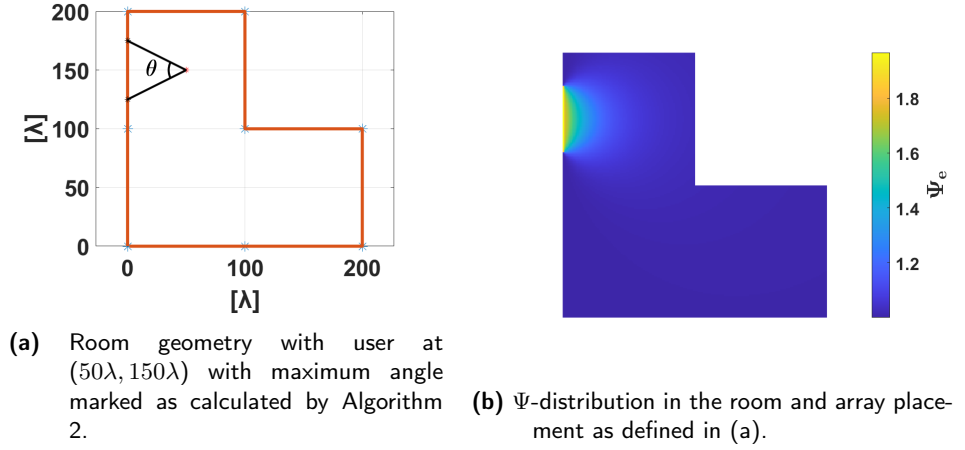


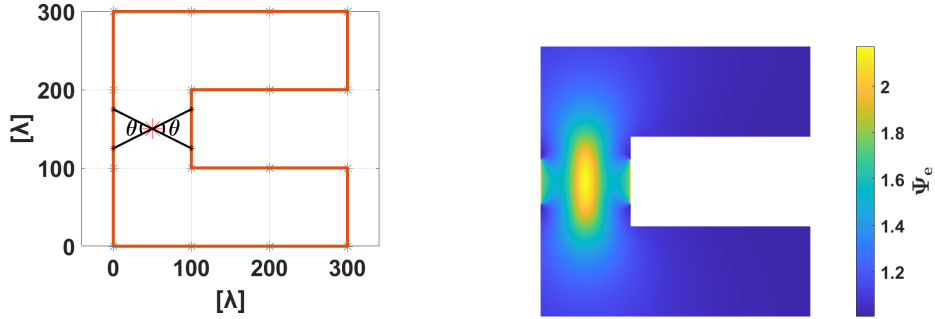
**Figure 4.14:** Performance metrics for a room with L-shaped geometry.

The exact implementation of Algorithm 2 is such that the primary array steps once for every full sweep of the walls of the secondary array. The iteration number for a wall with discretization of 101 points per wall segment would yield an unreadable figure and for illustration purposes, artistic freedom was taken by decreasing the graininess for a wall segment. The (now modified) full cumulative angle-iteration number relation for Fig. 4.15 (c) can be seen in Fig. 4.16.

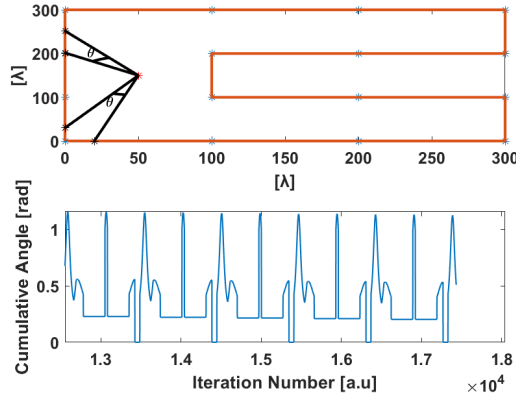
The pairwise two peaks of Fig. 4.16 are the optimal placements for the user for the room boundary in Fig. 4.15. This showcases the symmetry of the problem statement where, for an optimal solution, ULA 1 and ULA 2 are allowed to switch places for an equally valid solution. The plot of Fig. 4.15 (c) can be seen as a small segment of Fig. 4.16. Due to the complexity of portraying a truthful full overview of the cumulative angle plot, it will not be provided.

Previously, the user was placed in the middle of the defined rooms and therefore





(a) Room geometry with user at  $(50\lambda, 150\lambda)$  with maximum angle marked as calculated by Algorithm 2. (b)  $\Psi_e$ -distribution in the room and array placements as defined in (a).



(c) Cumulative angle for iterations number along the walls mid-calculation where the overlap of the arrays set the value to zero

**Figure 4.15:** Performance metrics for a room with C-shaped geometry.

a case for off-center placement is provided. For the same room as given in Fig. 4.14, the user was now placed at  $(75\lambda, 175\lambda)$  and results given in Fig. 4.17.

The resulting DoF-distribution for Fig. 4.17, where the user is placed off-centre imitates beamforming characteristics highlighting its relation to maximum spatial multiplexing. The resulting placement for the two ULAs is such that it occupies more than half of the FOV of the user, enveloping the user resulting in a higher spatial multiplexing at the user compared to other areas.

To be able to conclude the relation between solid angle and #DoF (here measured as  $\Psi_e$ ), the optimal array placement was calculated by optimising the #DoF metric  $\Psi_e$  which yielded the same placement of the ULAs. Therefore, for these test

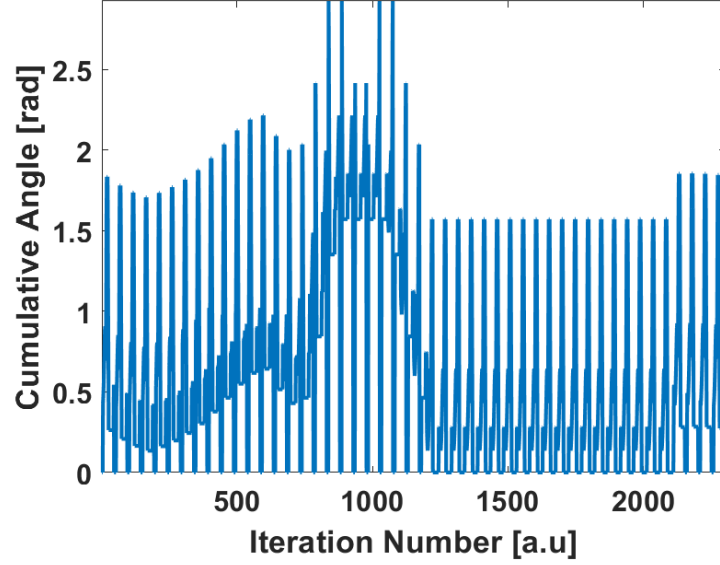
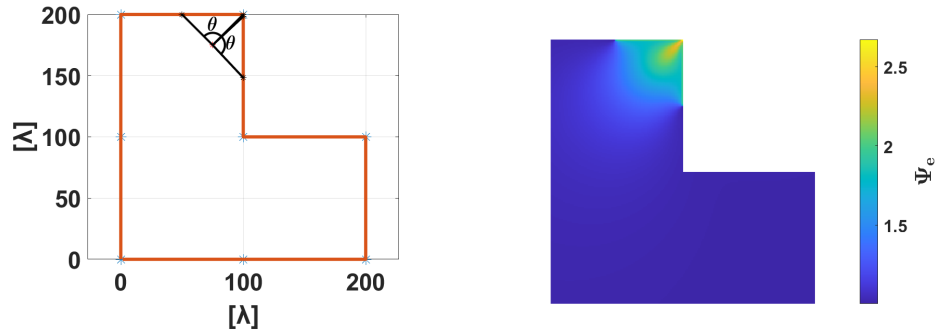


**Figure 4.16:** Total cumulative angle-iteration number calculation for boundary given in Fig. 4.15 (a) when iterating two identical ULAs.



**(a)** Room geometry with user at  $(75\lambda, 175\lambda)$  with maximum angle marked for two **(b)**  $\Psi_e$ -distribution for the room and array placements as defined in (a).

**Figure 4.17:** Performance metrics for a room with L-shaped geometry.

cases considering a single user, the behaviour of the DoF-distribution seems to suggest that maximising the solid-angle to the user, is equivalent to maximising  $\Psi_e$ . For the following cases, multiple users will be considered with the same antenna topology as used for the single user cases.

The rectangular room depicted in Fig. 4.13 is now revisited but with several users. Five users were placed in parallel to the long side of the room at height  $50\lambda$ . They were placed according to a closed uniform distribution with start and endpoint  $[10\lambda, 190\lambda]$ , which can be seen in Fig. 4.18.

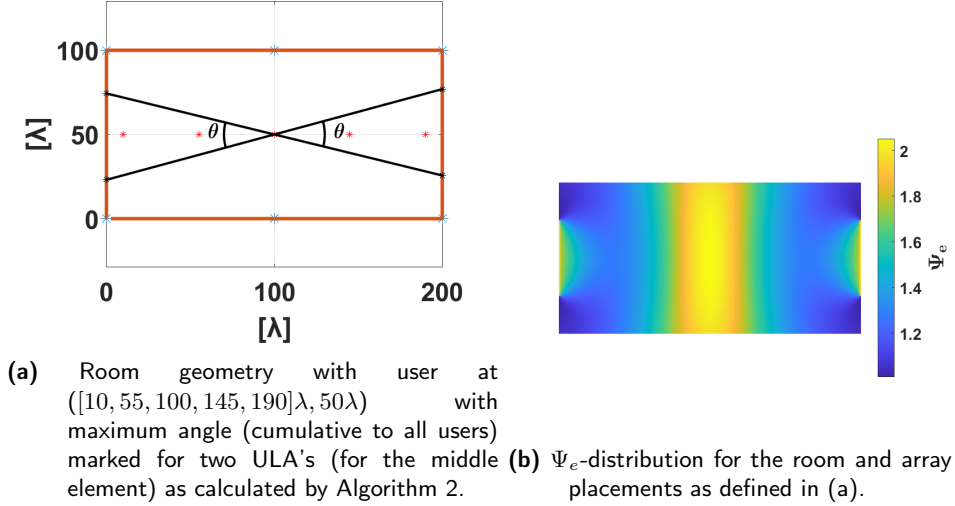


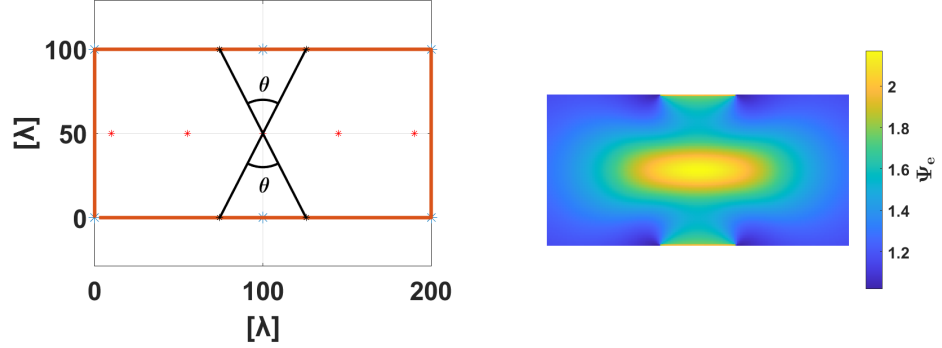
**Figure 4.18:** Performance metrics for a room with rectangular geometry.

The resulting DoF-distribution when maximising the cumulative angle in Fig. 4.18 suggests that for multiple users, the  $\Psi_e$  metric is high only for the user in the symmetric centre of the room. Instead optimising for maximal  $\Psi_e$  yields a placement of the ULAs such that several of the users are in the high spatial multiplexing region which is shown in Fig. 4.19.

The  $\Psi_e$  metric is calculated for the array placements in Fig. 4.18 and Fig. 4.19 which evaluates to  $\Psi_e = 3.7$  when optimising for maximum cumulative angle. Also,  $\Psi_e = 7.7$  when optimising for maximal  $\Psi_e$  metric. Therefore a counter-example has been found and it can be concluded that the maximum cumulative angle does not uniquely describe the maximal spatial multiplexing array placement for several users, whereas it does for a single user (in the provided test cases).

Since cumulative angle does **NOT** dictate the behaviour of the DoF-distribution for multiple users as shown in the previous counter-example, henceforth only the array placement which maximises the  $\Psi_e$  metric was considered.

Lastly, 17 volumetric users as visualised in Fig. 4.20 were considered in the L-shaped room in Fig. 4.17 (a). These users were evenly (in a good way) distributed to simulate a typical real-world scenario with many users and multiple BSs (two). This is referred to as a Multiple-User Multiple-input Multiple-output (MU-MIMO) scenario. The room with the users together with the resulting DoF-distribution is provided in Fig. 4.21.



(a) ULA placements which maximises  $\Psi_e$  for users at  $([10, 55, 100, 145, 190]\lambda, 50\lambda)$  for  $\Psi_e$  for the room and array placement as defined in (a). (b)  $\Psi_e$ -distribution for room that maximises  $\Psi_e$  for the room as calculated by Algorithm 2.

**Figure 4.19:** Performance metrics for a room with rectangular geometry.

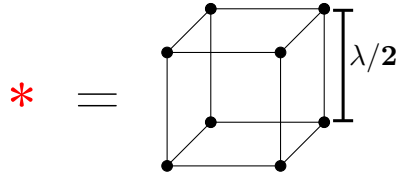


**Figure 4.20:** Cube layout of a user as 8 isotropic antennas on the vertices of a cube with side length  $\lambda/2$ .

Calculating the resulting  $\Psi_e$  metric for the setup in Fig. 4.21 with volumetric users as defined in Fig. 4.20 yields a value of  $\Psi_e = 17$ . The same setup applied to planar users yielded a value of  $\Psi_e = 13.6$ . The increase in spatial multiplexing when going from a planar user to a volumetric one indicates a great gain in capacity by introducing another describing dimension to the user which is more comparable to real-life scenarios. Note that due to the right diagonal symmetry of the problem, an equally good solution exists by mirror symmetry of the right diagonal.

To obtain a crude approximation of the gain in capacity, using only the  $\Psi_e$  metric, theory as described in Section 2.4.1 was used. This was done by using (2.15) and (2.4), which were derived as a consequence of the introduction of  $\Psi_e$ , and assuming that the modes are equally significant as described in the theory section 2.4.1. Calculation of the gain in capacity can be done in MATLAB as follows

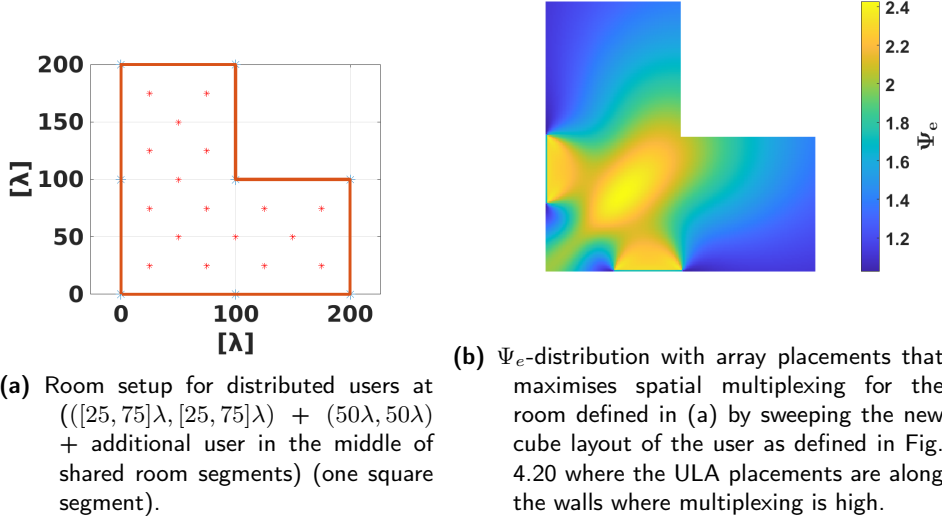


**Figure 4.21:** Performance metrics for a room with L-shaped room for Multiple User MIMO case.

```

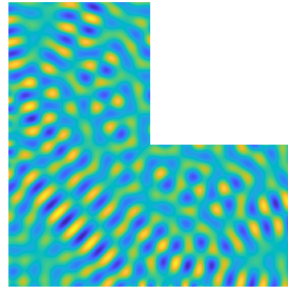
Psi_e = 17 %EDoF
SNR = 10^(20/10) ; %20 dB SNR
C1 = 1*log2(1+SNR);
C2 = Psi_e*log2(1+SNR/Psi_e) ;
res = C2/C1
%res = 7.1

```

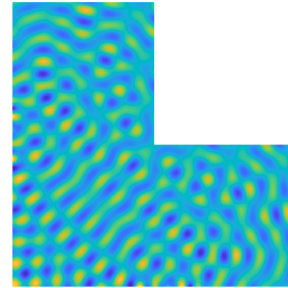
implying an over 7-fold increase in system capacity (compared to 6.3-fold for square user layout) if spatial multiplexing were to be used for the volumetric (cube) user.

To provide visualisation for the coupling of the modes for the MU-MIMO case in Fig. 4.21, artistic freedom was once again taken. The transmit vectors were taken from the solution when  $\lambda = 1$ . However, the propagating fields in Fig. 4.22 used  $\lambda = 15$ . This is because the placements of the ULAs differed if the simulated wavelength was altered. The increase in wavelength was made to be able to see the phase variations since a full  $2\pi$  phase shift is not discernible in a  $200\lambda \times 200\lambda$  layout.

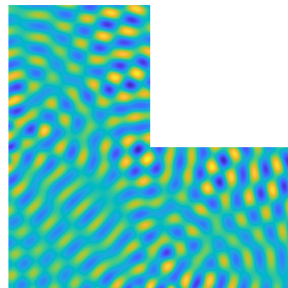
This methodology isn't just suitable for small, oddly shaped rooms; it's also applicable to large urban landscapes where obstacles and dense populations can impede telecom coverage. Algorithm 2 can be used to optimise for  $\Psi_e$ , which provides a computational method that suggests an effective placement of additional base stations, considering existing coverage areas.



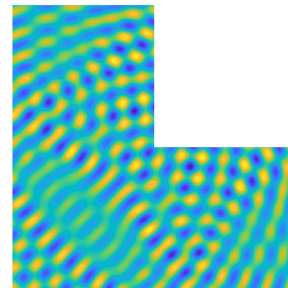
(a) Most dominant mode.



(b) Second most dominant.



(c) Third most dominant.



(d) Least dominant mode.

**Figure 4.22:** Visualisation for the three most dominant modes and least dominant mode for the square user layout.

---

## Conclusion & Future work

---

This thesis looked into research on spatial modes in the context of MIMO-systems by consolidating existing research as well as contributing novel insights. Through an extensive review of literature and original experimentation through computer simulation, this thesis confirms old findings and contributes to new ones. This thesis also introduces an analytically grounded metric and presents new results regarding the effects of apparent area (especially on the availability of spatial multiplexing for one as well as several users).

An exhaustive review of commonly used metrics for DoF estimation was conducted, highlighting both the similarities and differences among them, which assumptions and parameters they are based on and their applicability. Important parameters for increased spatial multiplexing are increased apparent area, small distance between BS and UE and an increased transmitted power (increased SNR  $\rho$ ) which enables positive contribution of previously unused modes.

It was shown that for single user MIMO, maximising for spatial multiplexing was the same as maximising for the solid angle between BS and UE. Further, it was shown that this relation does not hold for the case of MU-MIMO which encourages further research on the subject. Lastly, for MU-MIMO, the introduction of a volumetric receive topology showed gains in spatial multiplexing due to a more realistic UE description.

Arbitrarily placing out two BS's gave the possibility of optimising for high multiplexing in a certain region. Prior knowledge of preexisting placements of BS, in for example a city region, gives the algorithm presented herein a potential optimal suggestion on where to introduce an additional BS to efficiently provide service to users in a certain high traffic area.

Implementing a physics-based antenna model as a dipole decreased the spatial multiplexing capabilities, due to the antenna not being able to radiate in all directions, while simultaneously introducing a model more closely related to reality. Further examination is merited for other common antenna models and their impact on #DoF, such as patch antennas.

The dimensionality, #Tx and #Rx of the simulated problems were kept low for

computational complexity even after parallellising and vectorising the majority of the code. However, there is still merit in thoroughly investigating parameters such as antenna spacing (uniform and sparse) due to the existence of an optimal solution. However, considering the mutual coupling analysis and non-standard spacing makes for engineering problems where performance costs have to be considered and studied.

Beamforming characteristics were observed as a part of the solution for maximising spatial multiplexing for one of the test cases in the results chapter. Beamforming schemes are used in today's communications systems to in part increase signal strength together with reducing interference for other users [13]. The introduction of noise in the channel model would speculatively give a trade-off of the number of spatial modes together with beamforming to increase SNR to distinguish the modes from the introduced noise floor. The problem formulation of forming the channel matrix and optimising for capacity is a general optimisation problem not limited to spatial multiplexing.

Continuing with this thesis, the primary ongoing focus would be to integrate scattering effects into the models. Including these effects would make the algorithms more comparable to real-life scenarios (multipath) and enhances their practicality. Implementing scattering effects inherently involves integrating real-life antennas and polarization. With scattering effects in place, leading to greater spatial multiplexing [39], efforts to extend these effects to regions in the far field have been discussed, giving rise to the concepts of RIS and LIS [2, 10, 11, 15]. These surfaces can in part (simple example for intuition) reflect near-field modes from a user back to a distant BS. This makes it seem (from the BS point of view) that the signal emanates from the large surface which enables higher #DoF due to its larger size. If the surface is active, it can amplify the signal to achieve a higher SNR, further enabling more spatial modes to be used.

The maximum solid angle was proven useful for single user MIMO which merits further investigation into which design rules describe the availability of spatial multiplexing for multiple users since that would yield substantial advancement into the current understanding of how the DoF-distribution behaves and how to utilise it. Finally, extracting real-life data is essential to determine whether the theoretical findings in this report align with real-world observations.



## Maxwell's equations

---

The (Oliver) Heaviside [9] form of Maxwell's equations [16–18] are:

$$\nabla \cdot \mathbf{E} = \frac{\rho}{\varepsilon_0} \quad (\text{A.1})$$

$$\nabla \cdot \mathbf{B} = 0 \quad (\text{A.2})$$

$$\nabla \times \mathbf{E} = -\frac{\partial \mathbf{B}}{\partial t} \quad (\text{A.3})$$

$$\nabla \times \mathbf{B} = \mu_0 \mathbf{J} + \mu_0 \varepsilon_0 \frac{\partial \mathbf{E}}{\partial t} \quad (\text{A.4})$$

Where:

- $\mathbf{E}$  is the electric field vector, measured in volts per meter (V/m),
- $\mathbf{B}$  is the magnetic field vector, measured in teslas (T),
- $\rho$  is the charge density, measured in coulombs per cubic meter (C/m<sup>3</sup>),
- $\mathbf{J}$  is the current density, measured in amperes per square meter (A/m<sup>2</sup>),
- $\varepsilon_0$  is the vacuum permittivity, measured in farads per meter (F/m),
- $\mu_0$  is the vacuum permeability, measured in henries per meter (H/m),
- $\nabla$  is the nabla operator.

### A.0.1 Useful vector identities using $\nabla$ operator

We will utilise a few useful vector calculus identities:

$$\nabla \times (\nabla \times \mathbf{V}) = \nabla (\nabla \cdot \mathbf{V}) - \nabla^2 \mathbf{V} \quad (\text{A.5})$$

$$\nabla^2 \mathbf{V} = \nabla \cdot (\nabla \mathbf{V}) \quad (\text{A.6})$$

### A.0.2 Magnetic vector potential

One can define an arbitrary vector field and tailor it such that it can be used as an alternative way to solve for the electric field. This arbitrary field is called the magnetic vector potential [22]. It is defined as:

$$\mathbf{B} = \nabla \times \mathbf{A}, \quad \mathbf{E} = -\nabla \phi - \frac{\partial \mathbf{A}}{\partial t} \quad (\text{A.7})$$

Where:

- $\mathbf{A}$  is the magnetic vector potential which is just a vector field [Vs/m],
- $\phi$  is a scalar potential.

### A.0.3 Vacuum and charge-free version of Maxwell's equations

In the case of vacuum, charge-free and current free ( $\rho = 0, \mathbf{J} = 0$ ) space, Maxwell's equations becomes:

$$\nabla \cdot \mathbf{E} = 0 \quad (\text{A.8})$$

$$\nabla \times \mathbf{E} = -\frac{\partial \mathbf{B}}{\partial t} = -j\omega \mathbf{B} \quad (\text{A.9})$$

$$\nabla \cdot \mathbf{B} = 0 \quad (\text{A.10})$$

$$\nabla \times \mathbf{B} = \mu_0 \varepsilon_0 \frac{\partial \mathbf{E}}{\partial t} = j\omega \mu_0 \varepsilon_0 \mathbf{E} \quad (\text{A.11})$$

By taking the curl of the Electric-curl equation (A.9) yields:

$$\nabla \times (\nabla \times \mathbf{E}) = \nabla \times \left( -\frac{\partial \mathbf{B}}{\partial t} \right) = -\frac{\partial}{\partial t} (\nabla \times \mathbf{B}) = -\mu_0 \varepsilon_0 \frac{\partial^2 \mathbf{E}}{\partial t^2} \quad (\text{A.12})$$

Substituting everything to the same electric or magnetic field vector one obtains the EM-Wave Equation (for the electric field in this case):

$$\frac{1}{c_0^2} \frac{\partial^2 \mathbf{E}}{\partial t^2} - \nabla^2 \mathbf{E} = \mathbf{0} \quad (\text{A.13})$$

Where  $c_0$  is the speed of light in free space:

$$c_0 = \frac{1}{\sqrt{\mu_0 \varepsilon_0}} = 2.99792458 \times 10^8 \text{ m/s} \approx 3 \times 10^8 \text{ m/s} \quad (\text{A.14})$$

Solutions to the second order differential equations (A.12) are propagating waves that satisfy Maxwell's equations. Same equation manipulation can be performed to change out  $\mathbf{E}$  for  $\mathbf{B}$ . Example solutions are the following:

#### Spectral decomposition

Due to the linearity of Maxwell's equations in vacuum, solutions can be decomposed by a superposition of sine and cosine terms. The sinusoidal solution to the electromagnetic wave equation takes the form:

$$\mathbf{E}(\mathbf{r}, t) = \mathbf{E}_0 \cos(\mathbf{k} \cdot \mathbf{r} - \omega t + \phi_0) \quad (\text{A.15})$$

$$\mathbf{B}(\mathbf{r}, t) = \mathbf{B}_0 \cos(\mathbf{k} \cdot \mathbf{r} - \omega t + \phi_0) \quad (\text{A.16})$$

Where:

- $t$  is time [s],

- $\omega$  is the angular frequency [rad/s],
- $\mathbf{k} = (k_x\hat{\mathbf{x}} + k_y\hat{\mathbf{y}} + k_z\hat{\mathbf{z}})$  is the wave vector [1/m] and
- $\phi_0$  is the phase angle [rad].

The wave vector is related to the angular frequency by:

$$k = |\mathbf{k}| = \frac{\omega}{c} = \frac{2\pi}{\lambda} \quad (\text{A.17})$$

where  $k$  is the wavenumber and  $\lambda$  is the wavelength where  $\lambda f = c$  is utilised.

### Plane Wave solution

The plane wave solution, derived from spectral decomposition, offers a concise representation of electromagnetic fields for a single propagating wave. Suppressing the time dependence and relative phase, this solution takes on the following form:

$$\mathbf{E}(\mathbf{r}) = \mathbf{E}_0 e^{-j\mathbf{k}\cdot\mathbf{r}} \quad (\text{A.18})$$

$$\mathbf{B}(\mathbf{r}) = \mathbf{B}_0 e^{-j\mathbf{k}\cdot\mathbf{r}} \quad (\text{A.19})$$

#### A.0.4 The vector wave equation in non-chargefree space and its solution

By taking the curl of both sides of (A.2), utilising (A.4) and the vector identity (A.5) one obtains the vector wave equation for the  $\mathbf{E}$ -field.

$$\nabla \times (\nabla \times \mathbf{E}) = \nabla \times \left( -\frac{\partial \mathbf{B}}{\partial t} \right) = -\frac{\partial}{\partial t} (\nabla \times \mathbf{B}) = -\frac{\partial}{\partial t} (\mu_0 \mathbf{J} + \mu_0 \varepsilon_0 \frac{\partial \mathbf{E}}{\partial t}) \quad (\text{A.20})$$

Collecting L.H.S to R.H.S yields:

$$\nabla \times (\nabla \times \mathbf{E}) + \frac{\partial}{\partial t} (\mu_0 \mathbf{J} + \mu_0 \varepsilon_0 \frac{\partial \mathbf{E}}{\partial t}) = 0 \quad (\text{A.21})$$

Utilising that  $\frac{\partial}{\partial t} = j\omega$  (since time convention  $e^{j\omega t}$  is used) and moving the current to the R.H.S yields:

$$\nabla \times (\nabla \times \mathbf{E}) + \omega^2 \mu_0 \varepsilon_0 \mathbf{E} = -j\omega \mu_0 \mathbf{J} \quad (\text{A.22})$$

Finally using (A.17) and vector identity (A.5) yields:

$$(-\nabla \nabla \cdot + \nabla^2 + k^2) \mathbf{E} = -j\omega \mu_0 \mathbf{J} \quad (\text{A.23})$$

Note that  $\nabla \cdot \mathbf{E} = 0$ . Calculating the electric field from the magnetic vector potential then gives us the inhomogeneous Helmholtz equation:

$$(k^2 + \nabla^2) \mathbf{E} = -j\omega \mu_0 \mathbf{J} \quad (\text{A.24})$$

Notice the similarity to the solution to the inhomogeneous Helmholtz equation which is on the form:

$$\nabla^2 A(\mathbf{r}) + k^2 A(\mathbf{r}) = -f(\mathbf{r}) \quad \text{in } \mathbb{R}^n \quad n = 1,2,3 \quad (\text{A.25})$$

For the solution, boundary conditions are needed. One typically uses the Sommerfeld radiation condition [28]:

$$\lim_{r \rightarrow \infty} r \left( \frac{\partial}{\partial r} + jk \right) A(\mathbf{r}) = 0 \quad (\text{A.26})$$

With the Sommerfeld boundary condition, the solution takes the form of:

$$A(\mathbf{r}) = \int_{\mathbb{R}^3} G(\mathbf{r}, \mathbf{r}') f(\mathbf{r}') d\mathbf{r}' \quad (\text{A.27})$$

Similarly to the problem formulation of applied and induced currents, the integral is over a finite region, and  $G$  is the Green's function of this equation which satisfies:

$$\nabla^2 G(\mathbf{r}, \mathbf{r}') + k^2 G(\mathbf{r}, \mathbf{r}') = -\delta(\mathbf{r}, \mathbf{r}') \quad (\text{A.28})$$

By using  $n = 3$  of the Sommerfeld boundary condition, the Green's function takes the form:

$$G(\mathbf{r}, \mathbf{r}') = \frac{1}{4\pi} \frac{\exp(-jk_0|\mathbf{r} - \mathbf{r}'|)}{|\mathbf{r} - \mathbf{r}'|} = g(\mathbf{r}, \mathbf{r}') \quad (\text{A.29})$$

Real life propagation of electromagnetic-fields also carries a polarisation which the green's scalar function Eq. 2.2 lacks since it is scalar-valued. This study only focuses on examining how the DoF-distribution behaves and its influential parameters as the interest lies in maximising the bound of #DoF and not introducing orthogonal bases on which multiples of the function can be defined. By superpositioning three Green's function along the three unit vectors in  $\mathbb{R}^3$ , the Dyadic Green's formulation is achieved [3] (which includes the description of polarisation).

## Farfield Definition

---

An illustration of the Fraunhofer (farfield) distance can be seen in Fig. B.1. If we denote the distance between the line aperture with length  $D$  to the isotropic antenna denoted by a dot as  $z$ , then the extra distance travelled to the edge of the line aperture is  $\Delta$ . The relation can be expressed with the Pythagorean Theorem as  $(z + \Delta)^2 = z^2 + (\frac{D}{2})^2$ . Extracting  $\Delta$  from the expression yields:  $\Delta = z\sqrt{1 + (\frac{D}{2z})^2} \approx \frac{D^2}{8z}$  where the approximation utilises the first order Taylor expansion  $\sqrt{1 + x} \approx 1 + \frac{x}{2}$  which is valid for small  $x$ . The definition is such that this extra distance  $\Delta$  shall not give rise to a higher phase variation than  $\frac{\pi}{8}$ , i.e.  $\frac{2\pi}{\lambda}\Delta = \frac{\pi}{8}$ . The resulting limit for near and farfield is  $z = \frac{2D^2}{\lambda}$ .

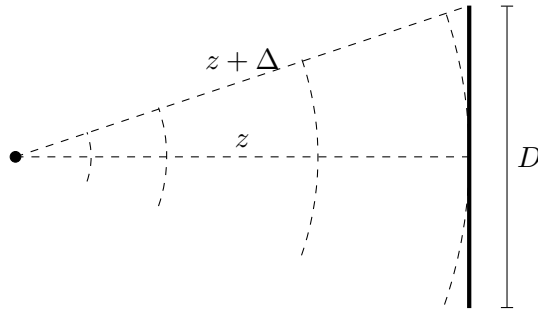


**Figure B.1:** Illustration of the Fraunhofer distance on how a beam has to travel longer to the edge of an aperture ( $+\Delta$ ) than to the middle of it, introducing a phase delay.



## Discretization schemes: Lebedev Quadrature

---

Uniformly placing out  $N$  points over a three-dimensional sphere is not uniquely defined. A scheme for placing out these points in a good way such that it is an approximation of the surface integral is the Lebedev quadrature [14].

The surface integral of a function over the unit sphere  $\mathbb{S}^2 = \{\mathbf{x} \in \mathbb{R}^3 : \|\mathbf{x}\|_2 = 1\}$  in  $\mathbb{R}^3$  is defined as

$$I[f] = \int_{\mathbb{S}^2} f(x) \, d\Omega = \int_0^{2\pi} \int_0^\pi f(\theta, \varphi) \sin(\theta) \, d\theta \, d\varphi \quad (\text{C.1})$$

which can be approximated by the Lebedev scheme as

$$\tilde{I}[f] = 4\pi \sum_{i=1}^N w_i f(\theta_i, \varphi_i) \quad (\text{C.2})$$

Where the weights  $w_i$  and grid points  $(\theta_i, \varphi_i)$  are to be determined. They are to be chosen such that they are invariant under the octahedral rotation group with inversion. Further description of this is outside of the scope of this thesis [14]. The main goal is to equalise every point such that they all have equal area and for the locations where this cannot be done, adjust the weights such that this inconsistency is mitigated.

Since Lebedev quadrature are more uniformly placed than  $(\theta, \varphi)$  distributed points, fewer points are needed for convergence. This leads to faster computation as many of the problems are sequential. Visualisation of the differences can be seen in Fig. C.1.

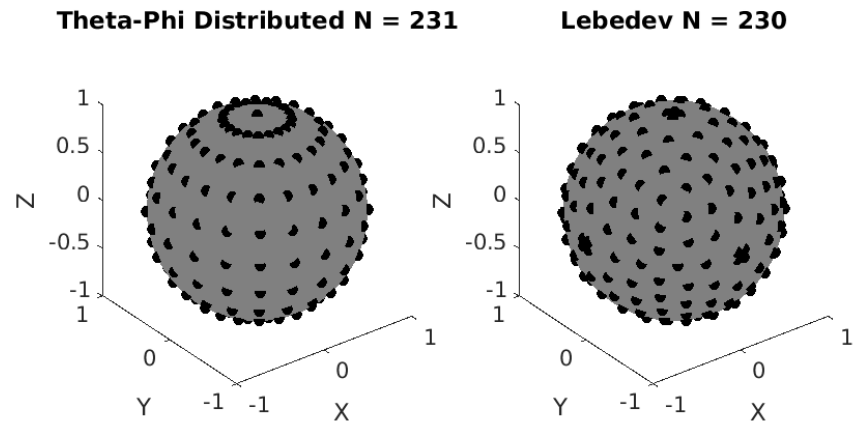


**Figure C.1:** Theta-phi distributed points (left) and lebedev distribution (right).



Appendix D

Pseudo Code

---

---

**Algorithm 1** Compute  $\Psi_e$  through Green's function matrix

---

**Require:** Matrix  $\mathbf{T}\mathbf{x}$  representing  $\mathbf{T}\mathbf{x}$  locations (in  $\mathbb{R}^3$ )

Matrix  $\mathbf{R}\mathbf{x}$  representing  $\mathbf{R}\mathbf{x}$  locations (in  $\mathbb{R}^3$ )

Scalar  $\lambda$  is the wavelength

1:  $N_s \leftarrow \text{length}(\mathbf{T}\mathbf{x}(:, 1))$

2:  $N_r \leftarrow \text{length}(\mathbf{R}\mathbf{x}(:, 1))$

3:  $\mathbf{distances} \leftarrow \text{zeros}(N_r, N_s)$

4: **for**  $i = 1$  to  $N_s$  **do**

5:    $\mathbf{distances}(:, i) \leftarrow \text{vecnorm}(\mathbf{T}\mathbf{x}(i, :) - \mathbf{R}\mathbf{x}, 2, 2)$

6: **end for**

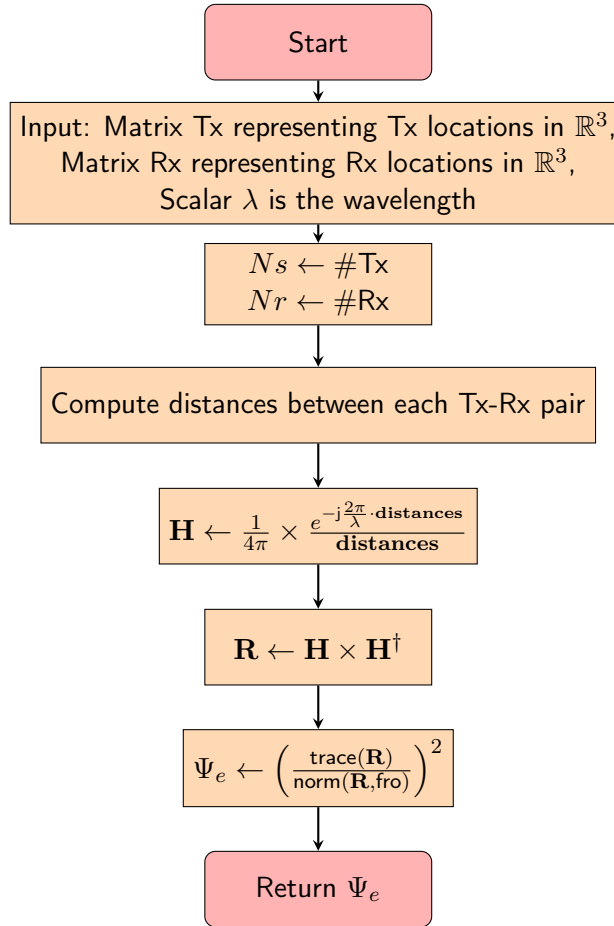
7:  $\mathbf{H}_q \leftarrow \frac{1}{4\pi} \times \frac{e^{-j\frac{2\pi}{\lambda} \cdot \mathbf{distances}}}{\mathbf{distances}}$

8:  $\mathbf{H} \leftarrow \text{reshape}(\mathbf{H}_q, [N_r, N_s])$

9:  $\mathbf{R} \leftarrow \mathbf{H} \times \mathbf{H}^\dagger$

10:  $\Psi_e \leftarrow \left( \frac{\text{trace}(\mathbf{R})}{\text{norm}(\mathbf{R}, 'fro')} \right)^2$

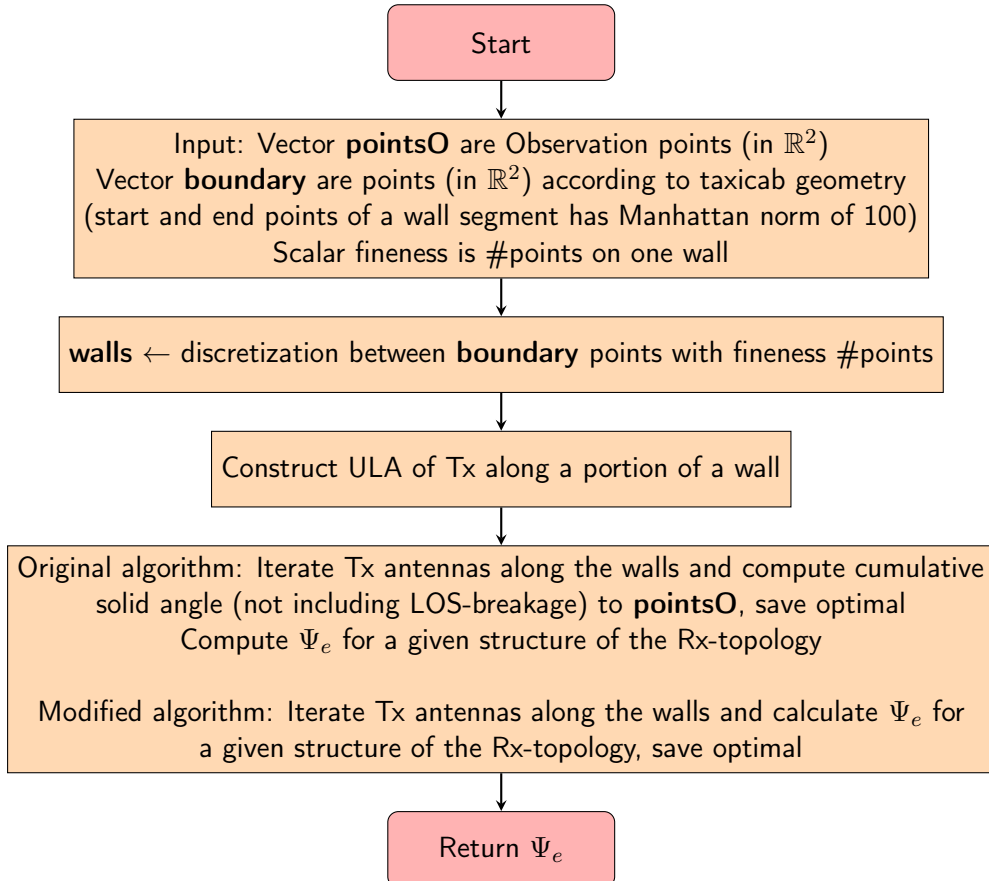
11: **return**  $\Psi_e$



**Algorithm 2** Compute Optimal Placement with respect to maximum angle

**Require:** Vector **pointsO** are Observation points (in  $\mathbb{R}^2$ )  
 Vector **boundary** are points (in  $\mathbb{R}^2$ ) according to taxicab geometry;  
 start and end of a wall segment has Manhattan norm of 100  
 Scalar fineness is #points on one wall

- 1: **walls**  $\leftarrow$  getWalls(boundary, fineness) {Discretization of walls}
- 2: **res**  $\leftarrow$  zeros(size(walls, 1), 1)
- 3: deltaIndex  $\leftarrow$  floor(fineness/2) {Tx is a portion of a wall-segment}
- 4: **for**  $i = 1$  to size(walls, 1): **do**
- 5:   index1  $\leftarrow$  i { start of array}
- 6:   point1  $\leftarrow$  walls(i, :)
- 7:   index2  $\leftarrow$  cyclicIndex(**walls**, i, deltaIndex) { end of array, walls are an Eulerian circuit }
- 8:   point2  $\leftarrow$  walls(index2, :)
- 9:   **for**  $k = 1$  to size(**pointsO**, 1): **do**
- 10:     pointOrigin  $\leftarrow$  **pointsO**(k,:)
- 11:     **if**  $\sim$ checkCollision(**boundary**, pointOrigin, point1, point2) **then**
- 12:       **continue** {Don't count it in the sum}
- 13:     **end if**
- 14:     **res**(i)  $\leftarrow$  **res**(i) + angle(pointOrigin, **walls**, point1, point2)
- 15:   **end for**
- 16: **end for**
- 17: **return** **res**





---

## References

---

- [1] Nicholas Bernstein. The coordination and regulation of movements. 1967. Pergamon Press, Oxford.
- [2] Emil Björnson, Chan-Byoung Chae, Robert W. Heath Jr., Thomas L. Marzetta, Amine Mezghani, Luca Sanguinetti, Fredrik Rusek, Miguel R. Castellanos, Dongsoo Jun, and Özlem Tugfe Demir. Towards 6G MIMO: Massive Spatial Multiplexing, Dense Arrays, and Interplay Between Electromagnetics and Processing, 2024. Preprint available at arXiv:2401.02844.
- [3] Anders Bondeson, Thomas Rylander, and Pär Ingelström. *Computational electromagnetics*. Springer, 2012.
- [4] Ray W. Clough. The finite element method after twenty-five years: A personal view. *Computers & Structures*, 12(4):361–370, 1980.
- [5] James W Demmel. *Applied numerical linear algebra*. SIAM, 1997.
- [6] Joseph G. Eisenhauer. Degrees of Freedom. *Teaching Statistics*, 30(3):75–78, 2008.
- [7] Andrea Goldsmith. *Wireless communications*. Cambridge university press, 2005.
- [8] Mats Gustafsson and Johan Lundgren. "Degrees of Freedom and Characteristic Modes", volume 7276 of *TEAT*. Lund University, May 2023.
- [9] Oliver Heaviside. *Electromagnetic theory*, volume 237. American Mathematical Soc., 2003.
- [10] Sha Hu, Fredrik Rusek, and Ove Edfors. The Potential of Using Large Antenna Arrays on Intelligent Surfaces. In *2017 IEEE 85th Vehicular Technology Conference (VTC Spring)*, pages 1–6, 2017.
- [11] Sha Hu, Fredrik Rusek, and Ove Edfors. Beyond Massive MIMO: The Potential of Data Transmission With Large Intelligent Surfaces. *IEEE Transactions on Signal Processing*, 66(10):2746–2758, 2018.
- [12] The MathWorks Inc. Signal propagation and targets toolbox, 2024.

- 
- [13] Per-Simon Kildal, Enrica Martini, and Stefano Maci. Degrees of Freedom and Maximum Directivity of Antennas: A bound on maximum directivity of nonsuperreactive antennas. *IEEE Antennas and Propagation Magazine*, 59(4):16–25, 2017.
- [14] Vyacheslav Ivanovich Lebedev. Values of the nodes and weights of quadrature formulas of Gauss–Markov type for a sphere from the ninth to seventeenth order of accuracy that are invariant with respect to an octahedron group with inversion. *Zhurnal Vychislitel’noi Matematiki i Matematicheskoi Fiziki*, 15(1):48–54, 1975.
- [15] Yuanwei Liu, Xiao Liu, Xidong Mu, Tianwei Hou, Jiaqi Xu, Marco Di Renzo, and Naofal Al-Dhahir. Reconfigurable Intelligent Surfaces: Principles and Opportunities. *IEEE Communications Surveys & Tutorials*, 23(3):1546–1577, 2021.
- [16] James Clerk Maxwell. A dynamical theory of the electromagnetic field. *Proceedings of the Royal Society of London*, (13):531–536, 1864.
- [17] James Clerk Maxwell. A dynamical theory of the electromagnetic field. *Philosophical transactions of the Royal Society of London*, (155):459–512, 1865.
- [18] James Clerk Maxwell. On physical lines of force. *Philosophical magazine*, 90(S1):11–23, 2010.
- [19] J.M. McCarthy and G.S. Soh. *Geometric Design of Linkages*. Interdisciplinary Applied Mathematics. Springer New York, 2010.
- [20] David A. B. Miller. Waves, modes, communications, and optics: a tutorial. *Adv. Opt. Photon.*, 11(3):679–825, Sept. 2019.
- [21] Tarik Muharemovic, Ashutosh Sabharwal, and Behnaam Aazhang. Antenna Packing in Low-Power Systems: Communication Limits and Array Design. *IEEE Transactions on Information Theory*, 54(1):429–440, 2008.
- [22] Franz Ernst Neumann. Allgemeine Gesetze der inducirten elektrischen Ströme. *Annalen der Physik*, 143(1):31–44, 1846.
- [23] Sophocles J Orfanidis. Electromagnetic waves and antennas. *Online website*, 2002.
- [24] Arogyaswami Paulraj, Rohit Nabar, and Dhananjay Gore. *Introduction to space-time wireless communications*. Cambridge university press, 2003.
- [25] Frederick Reif. *Fundamentals of statistical and thermal physics*. Waveland Press, 2009.
- [26] Claude Elwood Shannon. A mathematical theory of communication. *The Bell system technical journal*, 27(3):379–423, 1948.
- [27] Da-Shan Shiu, G.J. Foschini, M.J. Gans, and J.M. Kahn. Fading correlation and its effect on the capacity of multielement antenna systems. *IEEE Transactions on Communications*, 48(3):502–513, 2000.

- 
- [28] Arnold Sommerfeld. Die Greensche Funktion der Schwingungsgleichung. *Jahresbericht der Deutschen Mathematiker-Vereinigung*, 21:309–352, 1912.
- [29] David Tse and Pramod Viswanath. *Fundamentals of wireless communication*. Cambridge university press, 2005.
- [30] A.M. Tulino, A. Lozano, and S. Verdu. Impact of antenna correlation on the capacity of multiantenna channels. *IEEE Transactions on Information Theory*, 51(7):2491–2509, 2005.
- [31] S. Verdu. Spectral efficiency in the wideband regime. *IEEE Transactions on Information Theory*, 48(6):1319–1343, 2002.
- [32] V Vouk. Projected area of convex bodies. *Nature*, 162(4113):330–331, 1948.
- [33] Hermann Weyl. Über die asymptotische verteilung der eigenwerte. *Nachrichten von der Gesellschaft der Wissenschaften zu Göttingen, Mathematisch-Physikalische Klasse*, 1911:110–117, 1911.
- [34] Wikipedia. MIMO — Wikipedia, the free encyclopedia. <http://en.wikipedia.org/w/index.php?title=MIMO&oldid=1220742548>, 2024. [Online; accessed 06-May-2024].
- [35] Wikipedia contributors. Degrees of freedom — Wikipedia, the free encyclopedia, 2023. [Online; accessed 7-May-2024].
- [36] Wikipedia contributors. Joseph von fraunhofer — Wikipedia, the free encyclopedia, 2024. [Online; accessed 7-May-2024].
- [37] A.D. Yaghjian and Institute for Basic Standards (U.S.). Electromagnetics Division. *A direct approach to the derivation of electric dyadic Green's functions*. Number v. 13 in A Direct Approach to the Derivation of Electric Dyadic Green's Functions. Department of Commerce, National Bureau of Standards, Institute for Basic Standards, Electromagnetic Division, 1978.
- [38] Shuai S. A. Yuan, Zi He, Xiaoming Chen, Chongwen Huang, and Wei E. I. Sha. Electromagnetic Effective Degree of Freedom of an MIMO System in Free Space. *IEEE Antennas and Wireless Propagation Letters*, 21(3):446–450, 2022.
- [39] Xiao Qi Zhang, Rui Wen Shao, Hui Xu, Jun Wei Wu, and Tie Jun Cui. Electromagnetic Effective Degree of Freedom of MIMO System in Nonfree Space. In *2022 International Applied Computational Electromagnetics Society Symposium (ACES-China)*, pages 1–3, 2022.